Continuum effects for the low-lying states in drip-line oxygen isotopes

Koshiroh Tsukiyama

Department of Physics
University of Tokyo
January 31, 2008

Abstract

We investigate the continuum effects for the low-lying states in oxygen isotopes near the drip line. A continuum single-particle basis is introduced and shell-model calculation is performed using this basis in a small model space. The excitation strengths obtained are compared to those of experiments which have recently been performed. The contribution from the scattering states, especially from the resonance state, is clearly seen. The many-body perturbation theory to derive the effective interactions from the bare nucleon-nucleon potential is also discussed. These effective interactions are applied to the shell-model calculations with and without continuum effects in order to confirm the validity of our approach.

Contents

Chapter 1

Introduction

There are about 300 stable nuclei, whose properties have been well established, and about 6000 exotic nuclei, whose properties are mostly kept unknown. These exotic nuclei are extending on the nuclear chart out to the proton (neutron) drip line, where nuclei become unstable to proton (neutron) decay. Together with the development of the secondary exotic nuclear beams, the experimental methods to study the properties of exotic nuclei have spectacularly grown in all of the world, and the limits of nuclear existence are being explored. Nuclei far from the stability line grant nuclear physicists many interesting subjects. Among them, the nuclear shell structure at the drip lines is a fundamental question and plays an important role. In this thesis we investigate this problem, taking an example of oxygen isotopes near the drip line. In these nuclei, many unbound states start from low excitation energies, which implies that continuum states are important. Especially the most interesting phenomenon in continuum state is the resonance. What should be considered are how the continuum single-particle states affect the excitation strength of the very exotic nuclei and how these states have the influence to the effective interaction. These two are the main subjects in this thesis.

1.1 Treatments of resonance states

Drip-line physics, where nuclei with one or a few weakly bound states are concerned, is physics of threshold phenomena where both structure and reaction theory take place.

Therefore, the development of methods to deal with resonance and non-resonant continuum state in such nuclei plays a great important role. The characteristic feature of exotic states embedded in the continuum is that they can only exist for a finite time before they fall apart into their decay products. Such states are called quasi-stationary or resonant states. In a two-body picture, they can be understood as states trapped inside the centrifugal barrier for limited time, before they tunnel through the barrier and decay. Such resonant structures are often called shape resonances. Considering the time dependent wave function, which satisfies the Schrödinger equation for a complex energy $z = E_R - i\Gamma/2$,

$$\Psi(\mathbf{r}, t) = \Phi(\mathbf{r}) \exp(-izt/\hbar),$$

it is seen that the probability density,

$$|\Psi(\mathbf{r}, t)|^2 = |\Phi(\mathbf{r})|^2 \exp\left(-\Gamma t/\hbar\right),$$

decreases exponentially with time only for $\Gamma > 0$. This wave function is the only one which is appropriate to describe resonances or quasi-stationary states as pointed out by Gamow[1]. Resonances are observed in experiments as enhancements in the cross section when it is plotted as a function of energy. In the case of isolated resonances, where the peaks of resonances are well apart from each other in energies larger than their widths, and the resonances are far from decay thresholds, the total cross section over the resonance peak may be parameterized by the Breit-Wigner formula [2]. A detailed analysis of such data often reveals that this enhancement is due to one specific partial wave. In this sense, resonances have a definite set of quantum numbers just like bound states. What is different is the fact that these states have a definite lifetime and thus are the eigenstates with complex energies. This needs the extension of standard quantum mechanics which is formulated for Hermitian operators.

The study of two-body resonant structures has a long history in theoretical physics. A variety of methods has been developed for understanding the basic mechanisms of resonant states and processes taking place in the continuum, as explained in Refs. [3, 4, 5]. The common features in these methods are that they originate from standard scattering theory, and are based on the method of analytical continuation. Among the these methods are the complex scaling method (CSM) and the method based on analytic continuation in the

coupling constant (ACCC)[6, 4]. The CSM was originally formulated by Aguilar, Balslev and Combes in the early 70's [7, 8] and developed to examine the spectrum of the Green's function on the second energy sheet. Later this method has been applied to other fields such as atomic and molecular fields for the study of resonances. As an application of complex coordinate scaling to quantum chemistry, Moiseyev [9, 10] developed a generalized complex variational principle for resonant states. During the last fifteen years the CSM has also been applied in nuclear physics [11, 12, 13] for an application to loosely bound nuclear halo systems.

Another method is based on deforming contour integrals in momentum space, known as the contour deformation method (CDM) and, is closely related to the CSM. As shown by Afnan[14], a rotation of the integration contour in the lower half complex k-plane is equivalent to the complex coordinate rotation method, i.e. the CSM. The CDM allows us to consider a generalized type of contour, performing an analytic continuation into the lower half complex k-plane. Antibound and capture states near the scattering threshold may then be calculated.

The important question arising here is whether the resonant states obtained above can be a part of a complete set of states, since in nuclear physics, the expansion of many-body wave functions on single-particle basis generated by a suitable potential has been a common practice. In the late 60's Berggren proved that for a finite range potential, a finite set of bound and resonant states together with a set of non-resonant continuum states form a complete set [15] of bi-orthogonal functions, the normalization of which follows the generalized c-product [16, 9].

$$\mathbf{1} = \sum_n |\psi_{nl}\rangle\langle\psi^*_{nl}| + \int_{C^+} dk k^2 |\psi_l(k)\rangle\langle\psi^*_l(k)|, \quad \langle\langle\psi_{nl}|\psi_{n'l}\rangle\rangle \equiv \langle\psi^*_{nl}|\psi_{n'l}\rangle = \delta_{nn'}. \tag{1.1}$$

This representation is now known as the Berggren basis. C^+ is an arbitrary distortion of the positive real k-axis into the fourth quadrant of the complex k-plane. The non-resonant continuum integral is defined along a contour C^+, and the discrete sum is over bound, antibound and resonant states. The complete basis may be used to expand other states which belong to another Hamiltonian, and one can deduce the corresponding eigenvalue problem $H|\psi\rangle = E|\psi\rangle$. In this case, H is skew symmetric, not Hermitian.

1.2 Shell-model approach to nuclear structure

In nuclear physics one would ideally like to start from nucleon degrees of freedom. The underlying philosophy is that the nucleus, at low energies, can be fully described in terms of the the interactions between these constituents. Constructing the nucleus from nucleons and their mutual interactions, the quantum mechanical description of the many-body system however becomes extremely complex and difficult to deal with as the number of nucleons increases.

In the history of nuclear structure, the nuclear shell model has been very successful in describing properties of nuclei near the valley of stability. The shell model starts from the truncation of the Hilbert space. A truncated space is called a model space (or P-space), and only valence particles in the model space are treated as degrees of freedom. These particle interact each other through effective interaction, not through the bare nucleon-nucleon force. In the framework of ordinary shell model, single-particle wave functions are described as the eigenfunction of the harmonic oscillator potential. This is of course appropriate for the stable nuclei where each nucleon is assumed to be well confined and the amplitude of the single-particle wave functions rapidly decrease outside the surface. The harmonic oscillator wave functions are also favorable as they are well known mathematical functions. However, the possibly most attractive aspect is that the Hamiltonian which describes the motion of two particles in a harmonic oscillator potential can be written in separable form of two parts. One is relative and center-of-mass coordinates, and the other is laboratory coordinates. This makes the actual calculations feasible since the two-body effective interaction between the nucleons is given in relative coordinates.

When it comes to the neutron (proton) drip line, however, the situation is different. Nuclei cease to bound well, and harmonic oscillator representation of single-particle states loses the validity. Both the ground states and the distribution of the excitation strength can not be described by the ordinary shell model in the neutron rich region. These quantities can be explained by the continuum coupling in which not only resonant states but also non-resonant continuum states are mixed through the residual interaction. Intuitively one might expect that the Slater determinant built from single-particle resonances only would be the major component in the fully correlated many body wave function. This is

certainly true if the residual nucleon-nucleon interaction is negligible compared with the mean-field in which the valence particles move. What is more interesting is the opposite case, where the residual interaction is rather strong. In this case it is not obvious that the pure pole configurations are the most important. Some models may provide an answer to the question of how exotic structures, such as multi-particle resonances, embedded in the continuum are formed. Among them is Gamow shell model[17, 18, 19, 20, 21], starting from the Berggren representation in Eq. (1.1) for single-particle states. A complete many-body Berggren basis is then constructed from the discretized[*1] single-particle Berggren orbitals. Although their treatment of continuum single-particle states is quite accurate, they adopt the surface delta (Gaussian) interaction with adjusted parameters is taken as an effective two-body interaction. In Ref. [21] a renormalized nucleon-nucleon interaction is used for the two-body part of the Hamiltonian. Even so, the effective interaction is first oder in the sense of perturbation. Thus Gamow shell model is not a absolutely microscopic approach which contain the continuum effects. The final goal is to construct the method which deals with continuum single-particle states and takes into account the bare nucleon-nucleon interaction properly.

As a first stage, our framework is rather simple and straightforward, but can effectively take into account the whole continuum states. We focus on the drip-line oxygen isotopes, where configurations are described mainly in the *sd*-shell ($0d_{5/2}, 0d_{3/2}, 1s_{1/2}$). The oxygen isotopes are the heaviest nuclei for which the neutron drip line has been experimentally established [22]. The ground states of nuclei inside the drip line have lifetimes which are typical of those for β decay (a few hundred milliseconds in this mass region), and those outside the drip line have lifetimes which are characteristic of the strong interaction of unbound neutrons with nuclei (10^{-21}s). Typical direct measurements can identify nuclei with lifetimes longer than 10^{-9}s. Thus, the neutron drip line can experimentally be determined as the boundary between directly observed and non-observed nuclei. It has been revealed that nuclei up to ^{24}O are inside the drip line and that ^{25}O [23, 24] ^{26}O[25, 26], ^{27}O [27] and ^{28}O [27, 28] are outside the drip line.

[*1] Many-body slater determinants are constructed from the discrete bound, resonant and non-resonant continuum orbitals.

1.3 Outline of the thesis

This thesis falls into five chapters. After the above introductory remarks, we discuss about the shell-model calculation with continuum $d_{3/2}$ orbits in Chapter 2. The construction of continuum $d_{3/2}$ orbits and the phenomenological Hamiltonian are explained. Then, in Chapter 3, numerical results for oxygen isotopes near the drip line are shown. Chapter 4 is devoted to a brief explanation about the renormalization of a realistic nucleon-nucleon interaction and perturbative many-body approaches based on time-dependent perturbation theory in order to derive the effective interaction $V_{\rm eff}$. We show the results of shell-model calculation using $V_{\rm eff}$ in Sect. 4.3. Moreover in Sect. 4.4, we apply the $V_{\rm eff}$ to the shell-model calculation with continuum $d_{3/2}$ orbits discussed in Chapter 2. We conclude this thesis with an overview and a discussion of perspectives for the future investigations based on Chapter 5.

Chapter 2

shell-model calculation with continuum effect

As mentioned in Sect. 1.2, one should take into account single-particle continuum states to the ordinary shell-model calculation, when we consider the drip-line nuclei. Throughout this thesis, our attention is mainly paid for the drip-line oxygen isotopes. Usually these nuclei are described in terms of valence neutrons in the *sd*-shell consisting of $0d_{3/2}, 0d_{5/2}$, and $1s_{1/2}$ orbits.

The ordinary shell model often starts with a harmonic oscillator wave functions representing the single-particle orbits. Since the harmonic oscillator potential is an infinite one, the tails in single-particle wave functions fall off rapidly. The harmonic oscillator basis may therefore be considered as applicable only for the bound nucleons. In order that the shell model works well even for nuclei far from the stability line, one should abandon the full use of the harmonic oscillator wave functions of the single-particle motion. One needs a modification and reformulation of the ordinary shell-model so that one can describe the scattering continuum states in loosely bound or unbound states. In our calculation, in order to prevent the complexity, we assume six neutrons in $0d_{5/2}$ orbit as an inert core, namely assuming ^{22}O core. Further we consider the filling configuration. Therefore, in the case of the ground states in ^{24}O, for example, the configuration is restricted to ^{22}O core plus $(\nu 1s_{1/2})^2$.

2.1 Constructing the continuum basis

Single-particle energies of nuclei change according to the numbers of protons and neutrons. As an example, the result from mean field calculation is shown in Fig. 2.1. The single-particle energies of neutrons in *sd*-shell are obtained through Hartree-Fock calculation with two different parameter sets of Skyrme-type interaction. The neutron number is fixed at $N = 16$, and horizontal axis means the number of protons. Thus, $Z = 14$ is corresponding to ^{30}Si, belonging to the stable nuclei, and $Z = 8$ is ^{24}O, being an exotic nucleus. From Fig. 2.1, one can clearly see that $0d_{3/2}$ orbit becomes loosely bound or unbound when the neutron excess becomes larger. In this case the description of the corresponding orbit in terms of the harmonic oscillator wave functions cannot be preferable, and one should treat properly the wave function of this orbit.

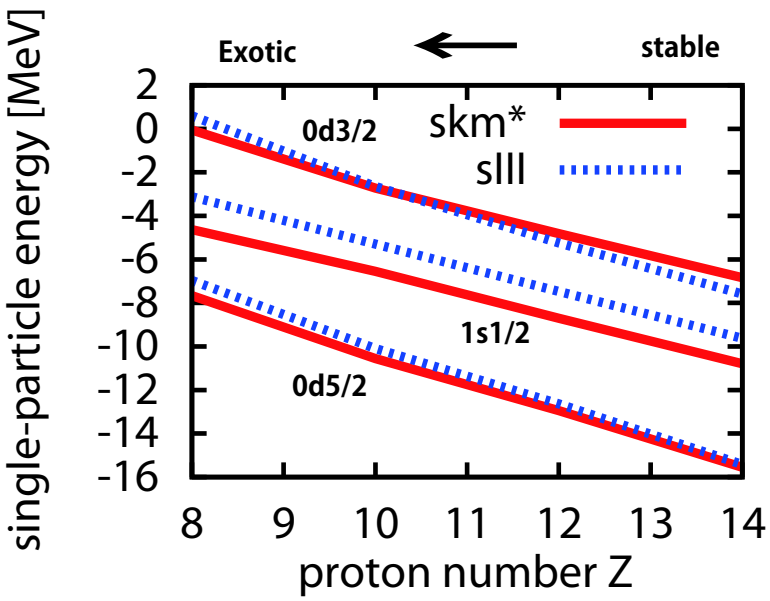

Figure 2.1: Changes of the single-particle energies of neutrons in *sd*-shell (N=16)

Therefore, we expand $0d_{3/2}$ orbit in terms of the eigenstates of an appropriate one-body potential. Our choice here is a Woods-Saxon potential. We generate the bound and continuum single particle states of $d_{3/2}$, solving Schrödinger equation with one-body

Hamiltonian,

$$H_0 = T + U_{\rm WS} + V_{\rm wall}, \tag{2.1a}$$

$$\text{where} \quad U_{\rm WS} = V_0 f(r) + V_{\rm LS}\frac{d}{dr}f(r), \quad f(r) = \left[1 + \exp\left(\frac{r-R}{a}\right)\right]^{-1}, \tag{2.1b}$$

$$\tag{2.1c}$$

$R = 1.09A^{1/3}$ is used. The V_0 is determined with $a = 0.67, V_{\rm LS} = -0.44V_0$, so as to satisfy the relation bellow.

$$\langle 0d_{3/2}|T + U_{WS}|0d_{3/2}\rangle = \tilde{\epsilon}_{0d3/2}(= 2.217\text{MeV}), \tag{2.2}$$

where $|0d_{3/2}\rangle$ means the harmonic oscillator wave functions, and $\tilde{\epsilon}_{0d3/2}$ is corresponding to the single-particle energy of $0d_{3/2}$ orbit in our model space $(\nu 0d_{3/2}, \nu 1s_{1/2})$. Further detail about the determination of $\tilde{\epsilon}_{d3/2}$ will be discussed in Sect. 2.2. Eq. (2.2) means that the single-particle energy of $d_{3/2}$ state becomes equal to $\tilde{\epsilon}_{d3/2}$ when described by the harmonic oscillator wave function. $V_{\rm wall}$ is an infinitely large wall, added to discretize the spectrum obtained. The position of the wall is set at $L = 1000$[fm]. This is mainly because we would like to obtain enough level density around the resonance. One may be afraid that this is too extreme, but as we will show later the result is unchanged even when we change L up to several hundred fm. In the end we obtain the discretized continuum $d_{3/2}$ states,

$$|id_{3/2}\rangle, \qquad i = 1, 2, \cdots, n_{\rm max}, \tag{2.3}$$

where i denotes an each continuum orbit, and $n_{\rm max}$ is the number of the continuum basis, corresponding to the maximum energy[*1]. Many-body Slater determinants are constructed from the bound $1s_{1/2}$ and continuum $id_{3/2}$ orbits.

2.2 Effective interaction for our model space

There are basically two ways to obtain effective interactions $V_{\rm eff}$ for shell model.

[*1] Originally $n_{\rm max}$ is 3000 but it is truncated for the computational convenience. We of course checked the convergence about $n_{\rm max}$. The results are unchanged when we perform the calculation with $n_{\rm max} = 3000$ to 300.

(a) Assuming that there exists an effective interaction, and one writes down $V_{\rm eff}$ based on some general considerations, and then determines it so as to obtain good agreement between calculation and experiment.

(b) Using many-body perturbation theory.

The empirical shell-model can be classified as belonging to approach (a), and has been very successful in reproducing experimental energy levels. This indicate the general validity of the effective interaction approach, or the existence of such a $V_{\rm eff}$. As for the approach (b), so called $\hat{Q}$-box expansion with folding operation [29, 30, 31, 32] has been used to derive the effective interactions in several model spaces. This will be discussed in Chapter 4. This approach has been well established for many years, but one has to note that all the works have been done using the harmonic oscillator basis except some works [33][*2].

In our calculation, when we take the approach (b) with continuum $d_{3/2}$ basis, the calculation may become huge due to the large number of $d_{3/2}$ orbits and the fact that we cannot analytically calculate each vertex in $\hat{Q}$-box diagrams. Actually, the construction of $V_{\rm eff}$ using a Berggren basis (in Eq. (1.1)) is now in execution. It is not possible to apply the approach (b) to our calculations. Thus, we take the approach (a). We assume the Hamiltonian in our model space, which consists of $1s_{1/2}$ and $id_{3/2}$ ($i = 1, \cdots n_{\max}$).

$$H = \hat{H}_0 + \hat{V} \tag{2.4a}$$

$$= \sum_i \tilde{\epsilon}_i a_i^\dagger a_i + \frac{1}{4}\sum_{i,j,k,l} \bar{v}_{ij,kl} a_i^\dagger a_j^\dagger a_l a_k, \tag{2.4b}$$

$$\bar{v}_{ij,kl} = \langle ij|V|kl\rangle, \qquad |ij\rangle \equiv a_i^\dagger a_j^\dagger |c\rangle, \tag{2.4c}$$

$$V(\boldsymbol{r}_1, \boldsymbol{r}_2) = g_1(1 + a_1\sigma_1\cdot\sigma_2)e^{-r^2/d_1^2} + g_2(1 + a_2\sigma_1\cdot\sigma_2)e^{-r^2/d_2^2}, \tag{2.4d}$$

where $|c\rangle$ means ^{22}O core and $r \equiv |\boldsymbol{r}_1 - \boldsymbol{r}_2|$. The ranges of the central interaction d_1, d_2 are given $d_1 = 1.4, d_2 = 0.7$, and can be different. The remaining parameters and single-particle energies are determined so that the Hamiltonian in harmonic oscillator representation becomes the same as or very close to the Hamiltonian which is used in ordinary shell model. We here choose SDPF-M interaction[34] which has been constructed in *sdpf*-shell[*3]. This

[*2]This work is done to carry out an extended study of the Vary-Sauer-Wong effect, i.e. the slow convergence of the intermediate-state summation in individual $\hat{Q}$-box diagrams.

[*3]To be more precise, it is constructed in sd, $0f_{7/2}$ and $1p_{3/2}$ space.

interaction is a modification of well known USD interaction[35] , for the sake that the drip-line properties of oxygen isotopes can be reproduced. The prescription is as follows.

First, we modify slightly the SDPF-M interaction so that it reproduces more precisely one-neutron separation energy of ^{23}O measured in the experiments [36, 37], by changing the monopole interaction as

$$\delta\langle 1s_1 0d_5|V|1s_1 0d_5\rangle_{T=1} = -0.03\text{MeV}. \tag{2.5}$$

This is actually less than 5% modification of the original value. Second, we reproduce the calculations with the configuration mixing in terms of the filling configuration. What should be done is to define the single-particle energies and the two-body matrix elements in the model space, composed of only $1s_{1/2}$ and $0d_{3/2}$ orbits (not full *sd*-shell). So taking the filling configuration, we reproduce the energies of the low-lying states in $^{23-26}$O relative to ^{22}O which are calculated with modified SDPF-M (obtained in the first step above) considering the configuration mixing. The resulting single-particle energies and two-body matrix elements are

$$\tilde{\epsilon}_{s_{1/2}} = -2.752\text{MeV}, \tilde{\epsilon}_{d_{3/2}} = 2.217\text{MeV} \tag{2.6a}$$

$$\langle 1s_{1/2}0d_{3/2}|V_{SM}|1s_{1/2}0d_{3/2}\rangle_{J=1,2} = 0.740, -0.516\text{MeV}, \tag{2.6b}$$

$$\langle 1s_{1/2}1s_{1/2}|V_{SM}|1s_{1/2}1s_{1/2}\rangle_{J=0} = -1.319\text{MeV}, \tag{2.6c}$$

$$\langle 0d_{3/2}0d_{3/2}|V_{SM}|0d_{3/2}0d_{3/2}\rangle_{J=0} = -2.3\text{MeV} \tag{2.6d}$$

One can say that single-particle energies and two-body matrix elements above have information about full *sd*-shell calculation though they are defined in $(0d_{3/2}1s_{1/2})$ space.

The strength of Woods-Saxon potential (2.1) is determined using the value of $\tilde{\epsilon}_{0d3/2}$ in Eq. (2.6a). Finally, the parameters g_i, a_i are determined so that the matrix elements of ordinary shell model can be reproduced when we use the harmonic oscillator wave functions.

$$\langle 1s_{1/2}0d_{3/2}|V|1s_{1/2}0d_{3/2}\rangle_{J=1,2} = \langle 1s_{1/2}0d_{3/2}|V_{SM}|1s_{1/2}0d_{3/2}\rangle_{J=1,2} \tag{2.7a}$$

$$\langle 1s_{1/2}1s_{1/2}|V|1s_{1/2}1s_{1/2}\rangle_{J=0} = \langle 1s_{1/2}1s_{1/2}|V_{SM}|1s_{1/2}1s_{1/2}\rangle_{J=0} \tag{2.7b}$$

$$\langle 0d_{3/2}0d_{3/2}|V|0d_{3/2}0d_{3/2}\rangle_{J=0,2} = \langle 0d_{3/2}0d_{3/2}|V_{SM}|0d_{3/2}0d_{3/2}\rangle_{J=0,2} \tag{2.7c}$$

All the Vs in the l.h.s. of Eqs. (2.7) mean the interaction written in Eq. (2.4d). This means that our calculations become the same as the normal shell-model calculations when we employ the harmonic oscillator wave function for the $0d_{3/2}$ state. The parameterization above is rather easy because when one adopts harmonic oscillator wave functions for single-particle states and assumes Gaussian-type central force, the matrix elements can be readily evaluated analytically, using Racah algebra [38] and the method by Horie *et al.* [39]. This is actually one of the advantages of harmonic oscillator functions. In final expression, the matrix elements in harmonic representation are,

$$\begin{aligned}
&\langle 1s_{1/2}0d_{3/2}|V|1s_{1/2}0d_{3/2}\rangle_{J=1} \\
&\qquad = \sum_{i=1,2} g_i \left(1+\frac{a_i}{4}\right)\left[\ R^{(0)}(sd,sd;d_i) - R^{(2)}(sd,ds;d_i)\right] \qquad (2.8a)\\
&\langle 1s_{1/2}0d_{3/2}|V|1s_{1/2}0d_{3/2}\rangle_{J=2} \\
&\qquad = \sum_{i=1,2} g_i \left[\left(1-\frac{3a_i}{20}\right)\ R^{(0)}(sd,sd;d_i) - \left(\frac{1}{5}+\frac{9a_i}{20}\right) R^{(2)}(sd,ds;d_i)\right] \qquad (2.8b)\\
&\langle 1s_{1/2}1d_{1/2}|V|1s_{1/2}1d_{1/2}\rangle_{J=0} = \sum_{i=1,2} g_i \left(1-\frac{3}{4}a_i\right) R^{(0)}(ss,ss;d_i) \qquad (2.8c)\\
&\qquad\qquad\qquad \cdots\cdots ,
\end{aligned}$$

where $R^{(k)}$s in Eq. (2.8) are calculated using (A.18) as

$$R^{(0)}(sd,sd;d) = \frac{1}{90}\left[90J_0(d) - 120J_1(d) + 61J_2(d) - 14J_3(d) + J_4(d)\right] \qquad (2.9a)$$

$$R^{(2)}(sd,ds;d) = \frac{1}{90}\left[16J_2(d) - 8J_3(d) + J_4(d)\right] \qquad (2.9b)$$

$$R^{(0)}(ss,ss;d) = \frac{1}{36}\left[36J_0(d) - 48J_1(d) + 28J_2(d) - 8J_3(d) + J_4(d)\right] \qquad (2.9c)$$

and

$$J_m(d) = \frac{(m+1)!!}{2^m}\lambda^3(1+\lambda^2)^{-(m+3/2)} \quad \lambda = d\sqrt{\nu}, \quad \nu = \frac{m\omega}{2\hbar}, \qquad (2.10)$$

where $\hbar\omega$ is energy quantum, and m is a mass of neutron. Details of the calculations are written in Appendix A. Eventually parameters are obtained as follows,

$$g_1 = 8.00\text{MeV}, \qquad g_2 = -116\text{MeV}, \qquad a_1 = 4.60, \qquad a_2 = 1.40\ . \qquad (2.11a)$$

In this section, the determination of the Hamiltonian has been explained. Single-particle energies and two-body matrix elements in $(1s_{1/2}id_{3/2})$ space $(i = 1, \cdots n_{\max})$ is originated from SDPF-M, an effective interaction in ordinary shell model. We should note that there is another possibility. The Hamiltonian can be originated from an effective interaction which is microscopically deduced from the bare nucleon-nucleon interaction. This approach will be shown in Sect. 4.4.

Chapter 3

Numerical results for Low-lying states in $^{23-26}$O

3.1 Excited states of ^{24}O

For the purpose of describing the procedure of calculations of the excitation strength, we focus on the case of ^{24}O. The low-lying states of the other nuclei can be calculated in almost the same manner. In the framework of the shell model, we consider the filling configuration but $d_{3/2}$ state is expanded in terms of continuum single particle states obtained in Sec. 2.1. Therefore, the excited states of ^{24}O is a superposition of continuum basis represented by

$$|iJ^+\rangle = |1s_{1/2} \otimes id_{3/2}; J^+\rangle, \quad (J = 1, 2, \text{and } i = 1, \cdots, n_{\max}), \tag{3.1}$$

where $id_{3/2}$ means a continuum single particle state and i runs through the continuum basis. Since we consider the filling configuration, the number of shell-model states in J-scheme is only one in the oscillator representation, but we have $n_{\max}$ $d_{3/2}$ orbits in our space, thus the dimension of the Hamiltonian matrix is $1 \times n_{\max} = n_{\max}$. With this basis, we diagonalize the Hamiltonian matrix defined in Eq. (2.4). Then we get kth $|J^+\rangle$ states

$$|J^+_k\rangle = \sum_i^{n_{\max}} c_i^{(k)} |iJ^+\rangle = \sum_i^{n_{\max}} c_i^{(k)} |1s_{1/2} \otimes id_{3/2}; J^+\rangle. \tag{3.2}$$

The corresponding energy eigenvalues are E_k ($k = 1, \cdots n_{\max}$). To acquire the excitation strength, we consider the two-proton knockout reaction^{9}B(^{26}Ne,^{24} O)X which has

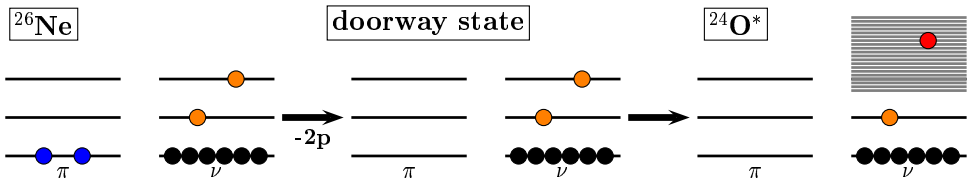

Figure 3.1: Schematic picture of the reaction^{9}B(^{26}Ne,^{24} O)X

actually been done in NSCL/MSU[*1][40]. A schematic picture of this reaction in configuration space is shown in Fig. 3.1. As an intermediate state between the initial and final states, we assume the doorway state where only two proton are removed from ^{26}Ne. Then whole reaction can be thought in two steps in Fig. 3.1. ^{26}Ne become the doorway state before it changes to the excited states in ^{24}O. Then a neutron is emitted just after the reaction when the low-lying states in ^{24}O, with the threshold energy E_k, are unbound. Since ^{26}Ne is bound nucleus, we can believe that a neutron in $0d_{3/2}$ orbit in the initial and the doorway states is represented by harmonic oscillator function. Hence one can consider that the emission probability is proportional to the squared overlap of these two states bellow

$$\text{Prob.}_k \propto |\langle 1s_{1/2}0d_{3/2}; J^+|J_k^+\rangle|^2 \propto \left|\sum_i c_i^{(k)} \left\langle 0d_{3/2}|id_{3/2}\right\rangle\right|^2 \equiv p_k. \tag{3.3}$$

We show in Fig. 3.2 the value of p_k in Eq. (3.3) for each angular momentum as a function of threshold energy E_k, the energy measured from the ground state of ^{23}O. We should note here that discreet data is smeared out so that the sum of p_k is equal to the integration of the curve in the figure. The vertical dashed-dotted lines mean the results of bound approximation, that is, ordinary shell-model calculation with SDPF-M interaction in filling configuration. Therefore, the corresponding energy is written as

$$E = E(^{24}\text{O}; J^+) - E(^{23}\text{O}; \text{g.s.}) = \tilde{\epsilon}_{0d3/2} + \langle 0s_{1/2}0d_{3/2}|V_{SM}|0s_{1/2}0d_{3/2}\rangle_J. \tag{3.4}$$

Curves in Fig 3.2 are the results with continuum effects where $0d_{3/2}$ orbit is considered as continuum state and the basis obtained in Eq. (2.3) is used. Two figures 3.2(a) and

[*1]National Superconducting Cyclotron Laboratory at Michigan State University, USA

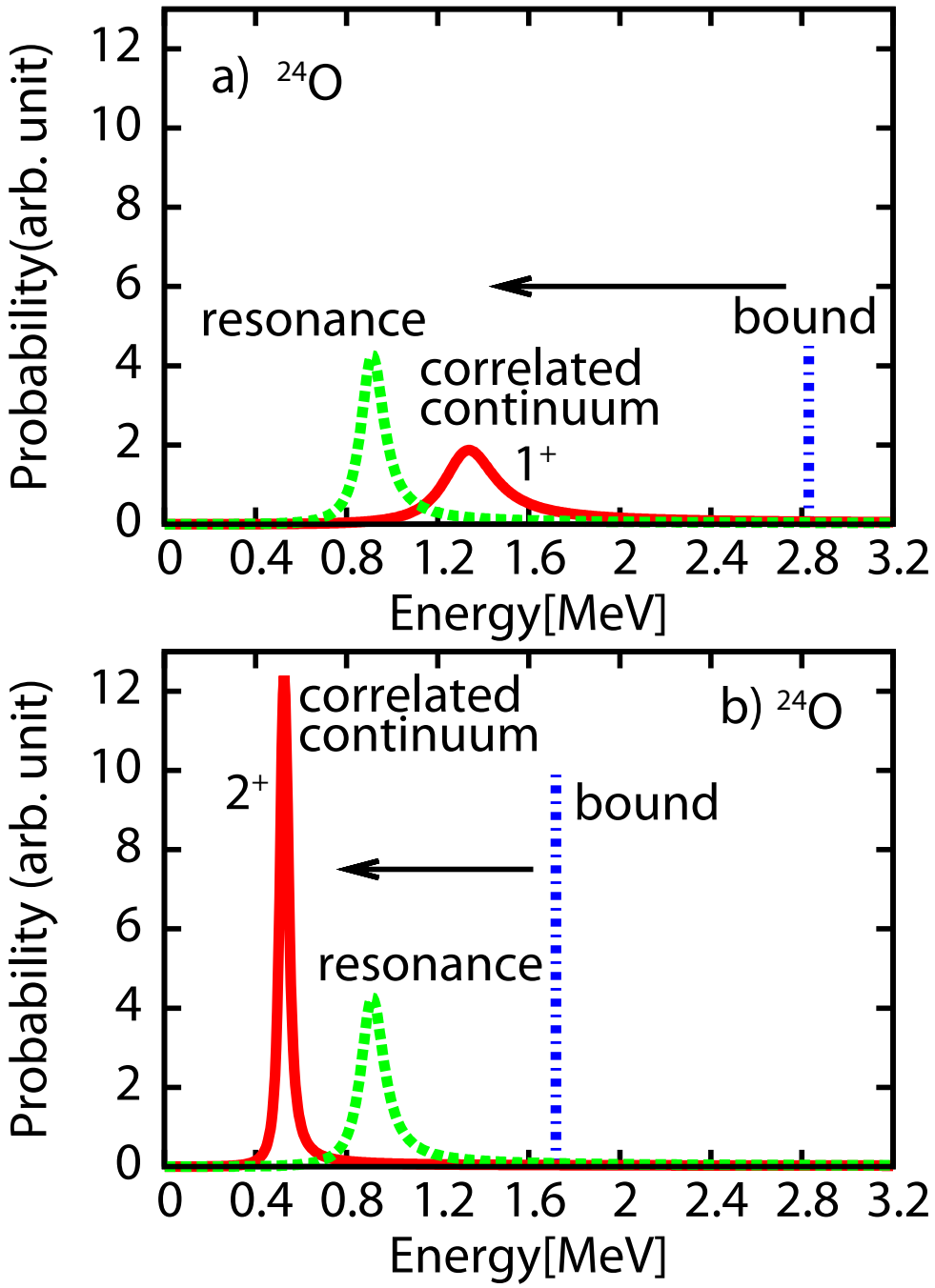

Figure 3.2: Overlap values p_ks of ^{24}O. (a) and (b) represent J^π=$1^+$and 2^+, respectively. The vertical dashed-dotted lines are the results of the normal shell-model calculation with filling configuration. The dotted curves correspond to the one particle resonance energy for ^{22}O core. And the solid curves are the results of the shell-model with continuum basis. One can see that the continuum coupled $1^+/2^+$ state is pushed up/down from the resonance. More details are written in the text.

3.2(b) represent 1^+ and 2^+ states in ^{24}O, respectively. The solid curves correspond to the results with Gaussian type interaction described Eq. (2.4d), and the dotted curves mean one neutron resonance for ^{22}O core. More precisely we calculate the quantity

$$\text{Prob.}_k \propto \left|\langle J^+|[0s_{1/2} \times kd_{3/2}]; J^+\rangle\right|^2 \propto \left|\langle 0d_{3/2}|kd_{3/2}\rangle\right|^2 . \tag{3.5}$$

One can see that the coupling with continuum states lowers the position of the peak by about 1 MeV, and these low-lying states are still unbound. We should take head that our result is consistent with the experiment[41, 40] in which no bound excited state was found in ^{24}O. As an important point, when we perform normal shell-model calculation in full *sd*-space, the results are not so different with that of $(1s_{1/2}0d_{3/2})$ model space. We show the results of shell-model calculation in full *sd*-shell, in addition to the results of the smaller space with and without continuum effect in Tab. 3.1. All the raws except "Present work" are the results of ordinary shell-model calculation with no continuum effects. "Bound app." corresponds to calculations performed in $(1s_{1/2}0d_{3/2})$ space, and "Full *sd*-space" means the shell-model calculation in the full *sd*-shell with three different effective interaction. Since in bound approximation, a shell-model state is restricted to the filling configuration, the main difference between "Bound app." and "Full *sd*-space" comes from the excitations from $1s_{1/2}$ orbit and $0d_{5/2}$ orbit, which is regarded as an inert core in $(1s_{1/2}0d_{3/2})$ space. One can understand, however, even when the excitations are considered, the spectrum is not so different. From the coupling to the continuum, on the other hand, the energies of low-lying states in ^{24}O are lowered and well reproduce the experimental tendency. One might feel that USDA[42] can well reproduce the experimental data. This is actually a modified version of USD, and based on a renormalized G-matrix with linear combinations of two-body matrix elements, but has been adjusted to fit a complete set of data for experimental binding energies and excitation energies for the *sd*-shell nuclei. One should note that in the new fit, recent data for the ground-state binding energies in $^{20-24}$O[43, 41, 44, 45] are used. Namely, effects of continuum are intended to be contained in two-body matrix elements.

	^{23} O		^{24}O		^{25}O	^{26} O	
States	$3/2^+$	$5/2^+$	1^+	2^+	$3/2^+$	0^+	2^+
Bound app.	2.22	-	2.83	1.72	2.17	4.09	4.24
Full *sd*-space							
SDPF-M	2.22	0.096	2.77	1.74	2.15	2.19	4.19
USD	0.54	-0.024	2.75	1.82	0.77	**-0.99**	1.33
USDA	1.51	0.035	1.75	1.06	1.32	0.51	2.46
Present work	**0.91**	-	**1.35**	**0.54**	**0.79**	**1.33**	**1.55**
Experiments	1.26	-	1.35	0.66	0.77	-	-

Table 3.1: Energy(from threshold)[MeV]

3.2 First excited state of ^{23}O

We show in Fig. 3.3 the results for other oxygen isotopes. The spin and parity of the ground state in ^{23}O is known to be $1/2^+$, and the configuration is $(\nu 1s_{1/2})(\nu 0d_{5/2})^6$[44][46], that is, one particle state in $(1s_{1/2}0d_{3/2})$ space. From the ordinary shell model (both SDPF-M and USDA), the first excited particle state is expected to be $3/2^+$ consisting of $(\nu 0d_{3/2})(\nu 0d_{5/2})^6$, while the first excited hole state is $5/2^+$ with $(\nu 1s_{1/2})^2(\nu 0d_{5/2})^5$ nearly around the threshold. Recently Elekes et al. [47] measured the low-lying excited states in ^{23}O by (d,p) reaction. They observed two excited states above the particle emission threshold, that is, the energy of the ground state of ^{22}O. The spins and parities of these excited states are $3/2^+$ at $E_x = 4.0$ [MeV], and $5/2^+$ at 5.3 [MeV]. $5/2^+$ state bellow the first $3/2^+$ resonance has not been observed in this experiment, although it is expected by the shell-model calculations. This is however reasonable because the first $5/2^+$ state should be populated by at least one neutron excitation from $0d_{5/2}$ orbit, which means this state is a hole state. Hole states are hard to see in (d,p) reaction. The $5/2^+$ states measured in this experiment is probably populated by the higher shell contribution like *pf*-shell. Since we regard six neutrons in $0d_{5/2}$ orbit as an inert core, we cannot describe the first $5/2^+$ states in our model space. Thus, we concentrate the first $3/2^+$ state. In this case there is only one valence neutron in our model space, therefore no residual interaction acts. What

one can see in this case is one particle resonance for ^{22}O core.

The result is shown in Fig. 3.3(a), where the dashed curve corresponds to one neutron resonance for the ^{22}O core, and the dashed-dotted vertical line means the result of ordinary shell model, namely the energy is nothing but the single-particle energy of $0d_{3/2}$ orbit since the horizontal axes is threshold energy. Experimental data is also plotted with solid curve. Even with no residual interaction, the threshold energy is lowered by more than 1 MeV just due to the coupling with the continuum, and rather well describes the experimental data.

3.3 Ground state of ^{25}O

As for ^{25}O, there are three valence neutrons in our model space. We diagonalize the Hamiltonian matrix with the same interaction given by Eq. (2.4), using the m-scheme basis represented by

$$|(1s_{1/2,1/2})(1s_{1/2,-1/2})(id_{3/2,3/2}); M = 3/2\rangle \quad (i = 1, \cdots, n_{\max}), \tag{3.6}$$

where single-particle states are denoted with angular momentum j and its z component. Since we now omit the excitation from $1s_{1/2}$ orbit, the configuration like

$$|(id_{3/2,1/2})(jd_{3/2,-1/2})(kd_{3/2,3/2}); M = 3/2\rangle \quad (i, j, k = 1, \cdots, n_{\max}) \tag{3.7}$$

is neglected. Therefore, total angular momentum can only be $J = 3/2$. After we obtain the $|3/2^+_k\rangle$ states, we assume the reaction of single proton striping from ^{26}F, namely, ^{9}Be(^{26}F,^{25} O)X. Here we can assume, by the same reason as for ^{24}O (discussed in Sec. 3.1), that the emission probability of a neutron is proportional to the squared overlap value p_k written in Eq. (3.3). The result is shown in Fig. 3.3(b). The notations of the figure is the same as that in ^{24}O. The $3/2^+$ state is lowered by about 1.5 MeV from the bound approximation due to the continuum coupling. The difference between the solid curve and the dotted curve is, however, very close to each other as compared to the case of ^{24}O. This difference comes from the residual interaction. Since $1s_{1/2}$ orbit is occupied[*2] in ^{25}O, the

[*2]Note that now we assume the filling configuration.

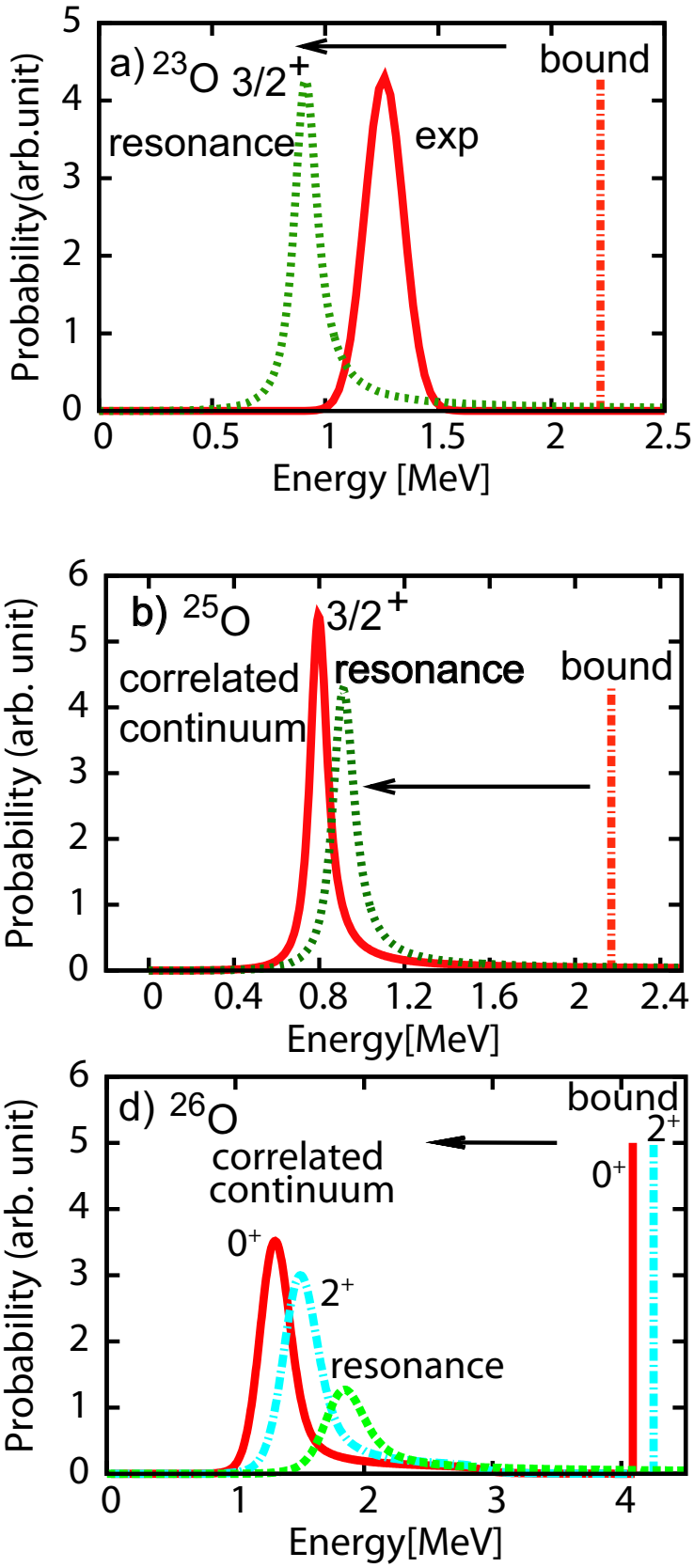

Figure 3.3: Overlap values p_ks as a function of threshold energy E_k.(a)-(c) corresponding to ^{23,25,26}O. All the notations are the same as that in Fig. 3.2.

interaction energy is nothing but the monopole term. In the filling configuration, assuming ordinary shell-model,

$$\begin{aligned} E(^{25}\mathrm{O}; 3/2^+) &= 2\tilde{\epsilon}_{1s1/2} + \tilde{\epsilon}_{0d3/2} + \langle (0s_{1/2})^2 | V | (0s_{1/2})^2 \rangle_{J=0} \\ &\quad + \frac{5}{4}\langle 1s_{1/2}0d_{3/2} | V | 1s_{1/2}0d_{3/2} \rangle_{J=2} + \frac{3}{4}\langle 1s_{1/2}0d_{3/2} | V | 1s_{1/2}0d_{3/2} \rangle_{J=1} \\ &= E(^{24}\mathrm{O}; \text{g.s.}) + \tilde{\epsilon}_{0d3/2} + 2\bar{V}^{T=1}_{1s1/2,0d3/2} \end{aligned} \tag{3.8}$$

Thus, the threshold energy is

$$E = E(^{25}\mathrm{O}; 3/2^+) - E(^{24}\mathrm{O}; \text{g.s.}) = \tilde{\epsilon}_{0d3/2} + 2\bar{V}^{T=1}_{1s1/2,0d3/2}, \tag{3.9}$$

where the monopole term of a two-body interaction between i and j orbits is defined as

$$\bar{V}ij^T = \frac{\sum_J (2J+1)\langle ij|V|ij\rangle_{J,T}}{\sum_J (2J+1)}, \tag{3.10}$$

which describes the average interaction between i and j orbits. Since two channels

$$\langle 1s_{1/2}0d_{3/2}|V|1s_{1/2}0d_{3/2}\rangle_{J=1,T=1}, \text{ and } \langle 1s_{1/2}0d_{3/2}|V|1s_{1/2}0d_{3/2}\rangle_{J=2,T=1}$$

are of the same order in magnitude and have opposite sign, the monopole term becomes small. Therefore, comparing Eqs. (3.4) and (3.9), $3/2^+$ state in ^{25}O can be very close to the single-particle energy of $0d_{3/2}$ orbit and the interaction energy is suppressed. This can be also the case even when the continuum basis is considered, and actually seen in Tab. 3.1. In Tab.3.1, the threshold energy of $3/2^+$ state in ^{23}O is corresponding to one-particle resonance for ^{22}O core in the case of "Bound app." and "Present work" since these calculation are done in $(1s_{1/2}0d_{3/2})$ space with the filling configuration[*3]. Looking at these threshold energies, $3/2^+$ states in ^{25}O are close to those in ^{23}O, while $1^+, 2^+$ states in ^{24}O are not.

The experiment about ^{25}O has recently been done in MSU[40] for the first time, using a proton knockout reaction from a ^{26}F beam as mentioned above. The threshold energy ,

[*3]See the raw "Bound app." and "Present work". Both correspond the calculation in $(1s_{1/2}d_{3/2})$ space, assuming the filling configuration. In the case of full-sd calculation, however, the situation is different since the interaction energy is a superposition of many matrix elements, not single channel.

that is the energy difference between the ground states of ^{24}O and ^{25}O, was found to be 770(20) keV with a total width of 172(30) keV in agreement with our calculation where the threshold energy is 790 keV, and the width is about 100 keV. One problem is that the width in our calculation is always smaller than that in experiments for all oxygen isotopes ^{23,24,25}O. This may be due to the fact that we restrict the model space to $(1s_{1/2}d_{3/2})$ and regard six neutrons in $0d_{5/2}$ orbit as an inert core. There are actually two contributions to the decay width: the "escape width" $\Gamma^{\uparrow}$, which is associated with the decay by particle emission, and the "spreading width" $\Gamma^{\downarrow}$ which measures the degree of fragmentation of the excitation strength due to mixing with complex configurations[48]. What has been calculated in current framework is the former. The width can be broaden if the core excitation is taken into account.

3.4 Low-lying states in ^{26}O

Lastly, we consider low-lying states in ^{26}O. In this case there are four valence neutrons in $(1s_{1/2}id_{3/2})$ space $(i = 1, \cdots, n_{\max})$. We again adopt the m-scheme and neglect the excitation from $1s_{1/2}$ orbit. Shell-model states in m-scheme representation in $M = 0$ space are written as

$$|\Psi_k; M=0\rangle = \sum_{i,j=1}^{n_{\max}} \Big[C_{ij}^{(k)} |1s_{1/2,1/2} 1s_{1/2,-1/2} id_{3/2,3/2} jd_{3/2,-3/2}\rangle + D_{ij}^{(k)} |1s_{1/2,1/2} 1s_{1/2,-1/2} id_{3/2,1/2} jd_{3/2,-1/2}\rangle \Big]. \tag{3.11}$$

The dimension of the Hamiltonian is $2 \times n_{\max}^2$ which makes the number of the matrix elements huge. Thus, calculations for ^{26}O have been done using the continuum basis obtained by the one-body Hamiltonian in Eq. (2.1a) with $L = 300$ fm, not 1000 fm, in order to reduce the value of $n_{\max}$. After the diagonalization, the coefficients $C_{ij}^{(k)}, D_{ij}^{(k)}$ in Eq. (3.11) are obtained. $M = 0$ space is divided into two subspaces with angular momentum $J = 0, 2$. After the angular momentum projection, one can obtain the wave

function with definite angular momentum.

$$|\Psi_k; J=0^+\rangle = \frac{1}{\sqrt{2}}\sum_{ij}(C_{ij}^{(k)} - D_{ij}^{(k)}) \left[|1s_{1/2,1/2}1s_{1/2,-1/2}id_{3/2,3/2}jd_{3/2,-3/2}\rangle \right.$$
$$\left. -|1s_{1/2,1/2}1s_{1/2,-1/2}id_{3/2,1/2}jd_{3/2,-1/2}\rangle\right], \tag{3.12}$$
$$|\Psi_k; J=2^+\rangle = \frac{1}{\sqrt{2}}\sum_{ij}(C_{ij}^{(k)} - D_{ij}^{(k)}) \left[|1s_{1/2,1/2}1s_{1/2,-1/2}id_{3/2,3/2}jd_{3/2,-3/2}\rangle \right.$$
$$\left. +|1s_{1/2,1/2}1s_{1/2,-1/2}id_{3/2,1/2}jd_{3/2,-1/2}\rangle\right]. \tag{3.13}$$

After the Hamiltonian matrix is diagonalized, one obtains the excitation strength considering the reaction ^{9}Be(^{28}Ne,^{26} O)X. We consider ^{28}Ne as a bound nucleus thus the two neutron emission probability p_k can be proportional to the overlap between the doorway state($|(\nu 1s_{1/2})^2(\nu 0d_{3/2})^2\rangle$) and continuum-coupled states.

$$p_k(J=0) \propto \left|\langle(1s_{1/2})^2(0d_{3/2})^2|\Psi_k; J^\pi=0^+\rangle\right|^2$$
$$\propto \left|\sum_{ij}^{n_{max}}(C_{ij}^{(k)} - D_{ij}^{(k)})\langle 0d_{3/2}|id_{3/2}\rangle\langle 0d_{3/2}|jd_{3/2}\rangle\right|^2 \tag{3.14}$$
$$p_k(J=2) \propto \left|\sum_{ij}^{n_{max}}(C_{ij}^{(k)} + D_{ij}^{(k)})\langle 0d_{3/2}|id_{3/2}\rangle\langle 0d_{3/2}|jd_{3/2}\rangle\right|^2 \tag{3.15}$$

The results of ^{26}O are shown in Fig. 3.3(c), where the solid lines represent 0^+ states for both bound approximation and continuum-coupled state, the dashed lines for 2^+ states, and the dotted line for the two particle resonance. The vertical lines are corresponding to the results of the bound approximation, that is, the ordinary shell model with filling configuration. In this case, $M=0$ space is spanned by the states

$$|\Psi_1\rangle = |0s_{1/2,1/2}0s_{1/2,-1/2}0d_{3/2,3/2}0d_{3/2,-3/2}\rangle, \tag{3.16a}$$
$$\text{and } |\Psi_2\rangle = |0s_{1/2,1/2}0s_{1/2,-1/2}0d_{3/2,1/2}0d_{3/2,-1/2}\rangle. \tag{3.16b}$$

One can readily obtain the wave functions with good angular momentum either by diagonalizing the Hamiltonian with the basis(Eq. (3.16)) or just using the angular momentum algebra.

$$|\Psi; 0^+\rangle = \frac{1}{\sqrt{2}}\left[|\Psi_1\rangle - |\Psi_2\rangle\right] \tag{3.17a}$$
$$|\Psi; 2^+\rangle = \frac{1}{\sqrt{2}}\left[|\Psi_1\rangle + |\Psi_2\rangle\right]. \tag{3.17b}$$

The corresponding energy eigenvalues are

$$\begin{aligned} E(^{26}\mathrm{O};0^+) &= 2\tilde{\epsilon}_{1s1/2} + 2\tilde{\epsilon}_{0d3/2} + \langle (1s_{1/2})^2|V|(1s_{1/2})^2\rangle_{J=0} + \frac{5}{2}\langle 1s_{1/2}0d_{3/2}|V|1s_{1/2}0d_{3/2}\rangle_{J=2} \\ &\quad + \frac{3}{2}\langle 1s_{1/2}0d_{3/2}|V|1s_{1/2}0d_{3/2}\rangle_{J=1} + \langle (0d_{3/2})^2|V|(0d_{3/2})^2\rangle_{J=0} \\ &= E(^{24}\mathrm{O};\mathrm{g.s.}) + 2\tilde{\epsilon}_{0d3/2} + 2\cdot 2\bar{V}^{T=1}_{1s1/2,0d3/2} + \langle (0d_{3/2})^2|V|(0d_{3/2})^2\rangle_{J=0} \qquad (3.18a) \\ E(^{26}\mathrm{O};2^+) &= E(^{24}\mathrm{O};\mathrm{g.s.}) + 2\tilde{\epsilon}_{0d3/2} + 2\cdot 2\bar{V}^{T=1}_{1s1/2,0d3/2} + \langle (0d_{3/2})^2|V|(0d_{3/2})^2\rangle_{J=2}. \qquad (3.18b) \end{aligned}$$

Hence, the threshold energies in the filling configuration are

$$\begin{aligned} E_{\mathrm{th}}(^{26}\mathrm{O};0^+) &= E(^{26}\mathrm{O};0^+) - E(^{24}\mathrm{O};\mathrm{g.s.}) \\ &= 2\tilde{\epsilon}_{0d3/2} + 4\bar{V}_{1s1/2,0d3/2} + \langle (0d_{3/2})^2|V|(0d_{3/2})^2\rangle_{J=0} \qquad (3.19a) \\ E_{\mathrm{th}}(^{26}\mathrm{O};2^+) &= 2\tilde{\epsilon}_{0d3/2} + 4\bar{V}_{1s1/2,0d3/2} + \langle (0d_{3/2})^2|V|(0d_{3/2})^2\rangle_{J=2}. \qquad (3.19b) \end{aligned}$$

The difference between two threshold energies is nothing but the difference between $J = 0$ and $J = 2$ channels of the matrix element $\langle (0d_{3/2})^2|V|(0d_{3/2})^2\rangle_J$. "Resonance" in Fig. 3.3(c) means the sum of single resonance energies of neutrons in $d_{3/2}$ orbits, assuming that they do not interact each other. Therefore the corresponding peak energy in ^{26}O is about twice as that in ^{23,24,25}O. The coupling to continuum lowers the threshold energies by about 3 MeV for both $0^+, 2^+$ states in ^{26}O, and these states are still unbound states. Unfortunately there is no experiment which measures the decay energies for ^{26}O, but will be performed in the near future.

3.5 Densities of neutrons

We also show the density of a neutron in $d_{3/2}$ orbit. A density $\rho(\boldsymbol{r})$ is defined as the expectation value of the operator

$$\hat{\rho}(\boldsymbol{r}) \equiv \hat{\psi}^\dagger(\boldsymbol{r})\hat{\psi}(\boldsymbol{r}) = \sum_{m,n} u^*_m(\boldsymbol{r})u_n(\boldsymbol{r})a^\dagger_m a_n, \qquad (3.20)$$

where $u_m(\boldsymbol{r})$ is the spatial wave function of the single-particle state with quantum number m. Since what is needed is radial distribution, it is natural to consider the density

$$\rho(r) \equiv \int d\Omega \rho(\boldsymbol{r}). \qquad (3.21)$$

This quantity is readily evaluated, in the case of ^{24}O for example,

$$^{24}\text{O: } \rho_k(r) = |\phi_{1s}(r)|^2 + \sum_{ij}^{n_{\max}} c^{i*}_{(k)} c^{j}_{(k)} \phi^*_{id}(r)\phi_{jd}(r) \equiv \rho_{1s}(r) + \rho_{kd}(r). \tag{3.22a}$$

Clearly, ρ_{kd} represents the density of a neutron in continuum $d_{3/2}$ orbits, and the subscript k, running from k=1 to $n_{\max}$, means this state is the kth eigenstate of the Hamiltonian with the threshold energy E_k. Similarly,

$$^{25}\text{O: } \rho_{1s}(r) = 2|\phi_{1s}(r)|^2, \rho_{kd}(r) = \sum_{ij}^{n_{\max}} c^{i*}_{(k)} c^{j}_{(k)} \phi^*_{id}(r)\phi_{jd}(r) \tag{3.22b}$$

$$\begin{aligned} ^{26}\text{O: } \rho_{1s}(r) &= 2|\phi_{1s}(r)|^2, \\ \rho_{kd}(r) &= \sum_{ijl}^{n_{\max}} \left[\left(C^{(k)}_{ij} - D^{(k)}_{ij} \right)^* \left(C^{(k)}_{lj} - D^{(k)}_{lj} \right) \phi^*_{id}(r)\phi_{ld}(r) \right. \\ &\quad \left. + \left(C^{(k)}_{ij} - D^{(k)}_{ij} \right)^* \left(C^{(k)}_{il} - D^{(k)}_{il} \right) \phi^*_{id}(r)\phi_{ld}(r) \right]. \end{aligned} \tag{3.22c}$$

We show the plot of $r^2\rho_{k_m d}(r)$ in Fig. 3.4, comparing to that of free particle and the one particle resonance for the mean potential by ^{22}O core[*4]. The subscript k_m means that the energy E_{k_m} corresponds to that of the peak in Fig. 3.2, 3.3. In Fig. 3.4, (a), (b) are 1^+ and 2^+ states in ^{24}O, (c) for $3/2^+$ state in ^{25}O, and (d) for $0^+, 2^+$ states in ^{26}O. In (a)-(c), the resonance and free wave functions are added with dashed and dotted lines, respectively. The vertical axis is described in the scale of common logarithm. One can see that basically the wave function of each state is similar to that of the resonance inside the nuclei, and it gradually gets close to the spherical Bessel function of the corresponding k value. When one looks at the region inside the nucleus in (a), the density of 1^+ state is smaller than that of the resonance, while in (b) the density of 2^+ state becomes lager. This difference is caused by the residual interaction. In (c), the density of $3/2^+$ state in ^{25}O is very close to that of the resonance, the reason of which can be that the residual interaction is only monopole term and its magnitude is very small as discussed in Sec. 3.3. One should note about ^{26}O that in this case $L = 300$ fm is used for the position of the infinite wall because

[*4] The resonant state and free-particle state are solved without an infinite wall V_{wall}. Normalization is done so that these wave functions satisfy the relation $\int_0^L dr r^2 |\psi(r)|^2 = 1$, where L is the position of the wall.

of the computational economy and might not be enough to describe properly the behavior of the wave function. One needs $n_{\max}$ corresponding to at least 20 MeV to sufficiently describe the single-particle states. When one takes $L = 1000$ fm, $n_{\max} \geq 300$ is needed. Then the dimension of the Hamiltonian matrix becomes $2 \times n_{max}^2 = 1.8 \times 10^5$, which makes the calculation of the matrix elements quite time consuming.

Anyway one can see that the largest contribution to each state is that from the resonance state, but the density of each state inside the nucleus is enhanced or suppressed, due to the residual interaction, from that of the resonance according to their spin.

In this chapter, several numerical results of the shell model with continuum $d_{3/2}$ basis are shown for oxygen isotopes near the neutron drip line. The coupling to the continuum states lowers the energy of the low-lying states in drip line oxygen isotopes by about one or a few MeV, and well describes the experiments. Although resonance is the most important contribution, each wave function changes from that of the resonance in and near the nuclear surface due to the residual interaction.

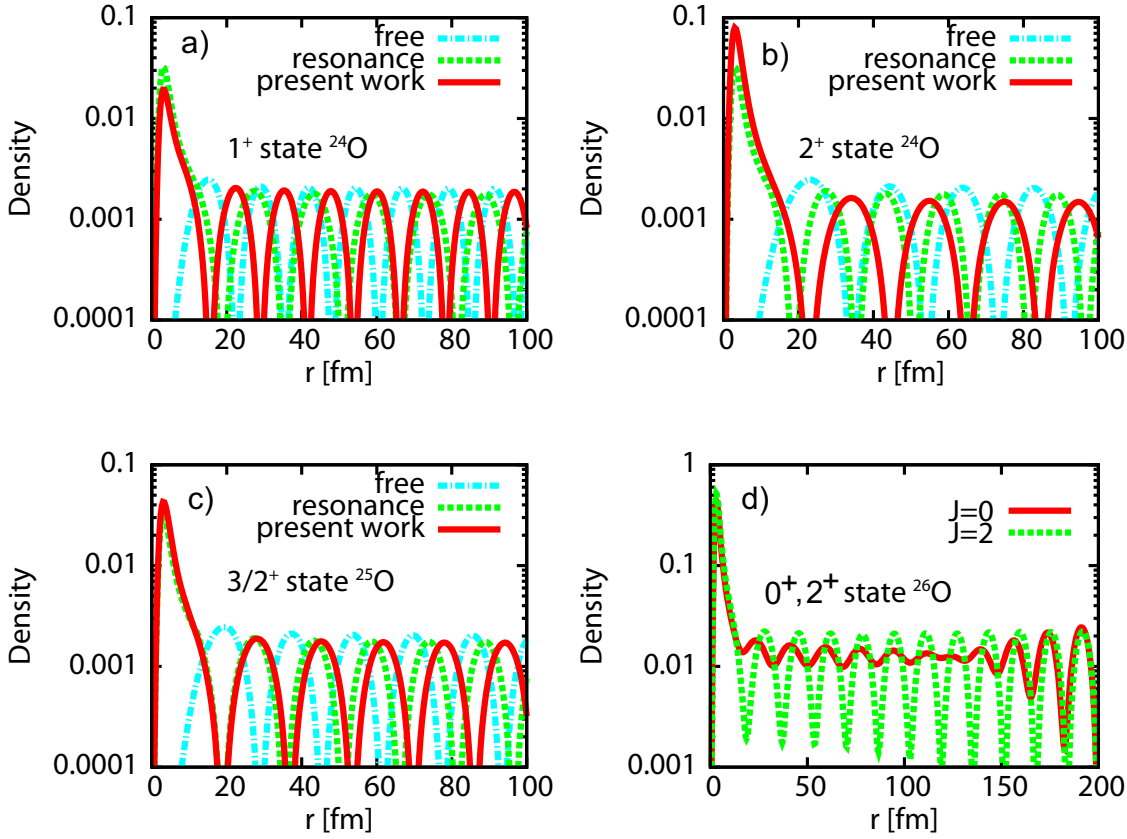

Figure 3.4: The radial distribution of the densities of neutrons in the continuum $d_{3/2}$ orbits, $\rho_{k_m d}(r)$ which correspond to the peaks in Fig. 3.2, 3.3. (a), (b) are 1^+ and 2^+ states in ^{24}O, (c) for $3/2^+$ state in ^{25}O, and (d) for $0^+, 2^+$ states in ^{26}O. In (a)-(c), the resonance and free wave functions are added by dashed and dotted lines, respectively. The vertical axis is described in the scale of common logarithm.

Chapter 4

Effective interaction derived from a realistic nucleon-nucleon potential

In the previous sections, the properties of the drip-line oxygen isotopes are well described by considering continuum single-particle wave functions in which scattering states especially resonance states are directly taken into account. The effective interaction is treated phenomenologically. More precisely, the parameters in our Hamiltonian are fixed so that the matrix elements can reproduce those of SDPF-M (ordinary shell model) when the harmonic oscillator wave functions are used for single-particle states. The reason why the Hamiltonian (2.4) in previous section is originated from SDPF-M interaction is that SDPF-M interaction can reproduce the drip-line properties of oxygen isotopes even in the framework of the ordinary shell-model calculations. With continuum effects, the better agreements with experiments are obtained. In this Chapter, another method will be taken in order to determine the parameters of the two-body part in the Hamiltonian (2.4). As mentioned in Sect. 2.2, there are basically two ways to obtain the effective interaction $V_{\rm eff}$ for the shell model. One approach is to parameterize $V_{\rm eff}$ with adjustable parameters (labeled as approach (a) in Sec. 2.2). This approach was done up to p-shell. The remarkably good results obtained with shell model indicate the general correctness of the effective interaction approach. The alternative approach is to derive $V_{\rm eff}$ from the first principle (labeled as approach (b) in Sec. 2.2). This approach has been developed considerably. However this approach may not be enough to describe precisely the observable. The drip line of

oxygen has not been reproduced using this approach. USD[-A] and SDPF-M have been constructed to complement the missing properties in the microscopic approach, adjusting a part of $V_{\rm eff}$ derived from the bare nucleon-nucleon interaction. We will show the outline of the latter method (approach (b)) in the following sections, and will apply the obtained two-body matrix elements to determine the Hamiltonian (2.4).

4.1 Brief outline of the effective interaction theory

Many-body problems start from the Schrödinger equation

$$H|\Psi_\lambda\rangle = E_\lambda|\Psi_\lambda\rangle, \tag{4.1}$$

where the Hamiltonian can be written as

$$H = T + V = (T + U) + (V - U) \equiv H_0 + H_1. \tag{4.2}$$

T is the kinetic energy and V a nucleon-nucleon interaction. The eigenfunctions Φ_i of H_0 are used, as a basis, for the expansion of the eigenfunction $|\Psi_\lambda\rangle$ of H. Thus, it is conventional to choose an arbitrary auxiliary one-body potential U which has an convenient mathematical form, typically harmonic oscillator potential is used. Since only a few low-lying states are generally of physical interest, the first thing one should do is to formulate the problem in terms of an effective interaction acting in a strongly truncated Hilbert space, i.e. a model space with a finite number of states. When low-lying states are concerned, one can expect the wave functions to be dominated by components with a closed core and nucleons in the valence orbit. Therefore, one can choose a model space spanned by the vectors bellow, in the case of two valence particles for instance,

$$|\Phi_i\rangle = \sum_{\alpha>\beta\in\text{valence shells}} C^{(i)}_{\alpha\beta} a^\dagger_\alpha a^\dagger_\beta |c\rangle, \qquad i = 1, \cdots, d, \tag{4.3}$$

where $|c\rangle$ is the unperturbed core constructed by completely filling the lowest orbits. It is convenient to define projection operators P which project the complete Hilbert space onto the model space. P can be represented in terms of the vectors in Eq. (4.3)

$$P = \sum_{i=1}^{d} |\Phi_i\rangle\langle\Phi_i|. \tag{4.4}$$

At the same time, Q is also defined as a projector onto the complementary space of P, that is, $P + Q = 1$. Using P, one can formally reduce the original eigenvalue problem in Eq. (4.1) to that in the model space, such as

$$PH_{\rm eff}P|\Psi_\lambda\rangle = E_\lambda P|\Psi_\lambda\rangle. \tag{4.5}$$

In ordinary shell model, one expects to have a model-space eigenvalue problem,

$$PH_{\rm eff}P|\Psi_\lambda\rangle = (E_\lambda - E_c)P|\Psi_\lambda\rangle, \tag{4.6}$$

where E_c is the true energy of the core. The effective Hamiltonian is then

$$H_{\rm eff} = H_0 + V_{\rm eff}, \qquad H_0 = \sum_\alpha \epsilon_a a^\dagger_\alpha a_\alpha. \tag{4.7}$$

ϵ_α is the binding energy with respect to the core. It is conventional not to calculate H_0, and ϵ_α are empirically taken as the binding energy difference between the state α in the nucleus in which there is one additional nucleon with the closed shells and the ground state of the corresponding closed-shell nucleus. In the shell model, $V_{\rm eff}$ is generally taken as pure two-body interaction even when there are more than two nucleon in the model space.

The effective interaction in a model space can be expressed as a perturbation series in terms of the nucleon-nucleon interaction, with either time-dependent or time-independent perturbation theory. This is formally exact. For the ground state of a closed-shell nucleus the energy shift from the unperturbed energy is given by the sum of all linked vacuum to vacuum diagrams. For nuclei with valence particles, $V_{\rm eff}$ is obtained by so-called $\hat{Q}$-box expansion with folding operation. Here we give a brief outline for the prescription, taking the time-dependent perturbation theory.

First, we define the parent states

$$|\rho_\lambda\rangle = \sum_{i=1}^{d} C_i^{(\lambda)}|\Phi_i\rangle, \qquad \lambda = 1, \cdots, d, \tag{4.8}$$

where $|\Phi_i\rangle$ means a model-space basis states. One should note that $|\rho_\lambda\rangle$ is entirety in a model space, that is, $P|\rho_\lambda\rangle = |\rho_\lambda\rangle$. If the projections $P|\Psi_\lambda\rangle$, $(\lambda = 1, \cdots, d)$, are linearly independent, then we can choose the coefficients in Eq. (4.8) so that

$$\langle P\Psi_\lambda|\rho_\mu\rangle = \langle\Psi_\lambda|\rho_\mu\rangle = 0, \quad \lambda \neq \mu. \tag{4.9}$$

From this condition, one can have the one-to-one correspondence between d parent states $|\rho_\lambda\rangle$ and the true eigenstates $|\Psi_\lambda\rangle$.

$$\frac{U(0,-\infty)|\rho_\lambda\rangle}{\langle\rho_\lambda|U(0,-\infty)|\rho_\lambda\rangle} \equiv \lim_{\epsilon\to+0}\lim_{t'\to-\infty(1-i\epsilon)} \frac{U(0,t')|\rho_\lambda\rangle}{\langle\rho_\lambda|U(0,t')|\rho_\lambda\rangle} = \frac{|\Psi_\lambda\rangle}{\langle\rho_\lambda|\Psi_\lambda\rangle}, \tag{4.10}$$

such that

$$H\frac{U(0,-\infty)|\rho_\lambda\rangle}{\langle\rho_\lambda|U(0,-\infty)|\rho_\lambda\rangle} = E_\lambda\frac{U(0,-\infty)|\rho_\lambda\rangle}{\langle\rho_\lambda|U(0,-\infty)|\rho_\lambda\rangle}. \tag{4.11}$$

Here $U(t,t')$ is the time-development operator[*1]. U is unitary and has the group property, and satisfies $U(t,t')U(t',t)=1$. In the complex-time limit one can write the perturbation expansion of the time-development operator $U(0,-\infty)$ in the interaction representation as[*2]

$$U(0,-\infty) = \lim_{\epsilon\to+0}\lim_{t'\to-\infty(1-i\epsilon)}\sum_{n=0}^{\infty}\left(\frac{-i}{\hbar}\right)^n\int_{t'}^{0}dt_1\int_{t'}^{t_1}dt_2\cdots\int_{t'}^{t_{n-1}}dt_n H_1(t_1)H_1(t_2)\cdots H_1(t_n). \tag{4.12}$$

Substituting Eq. (4.8) into Eq. (4.11), one obtains

$$\sum_{i=1}^{d}C_i^{(\lambda)}\frac{HU(0,-\infty)|\Phi_i\rangle}{\langle\rho_\lambda|U(0,-\infty)|\rho_\lambda\rangle} = \sum_{j=1}^{d}C_j^{(\lambda)}\frac{E_\lambda U(0,-\infty)|\Phi_j\rangle}{\langle\rho_\lambda|U(0,-\infty)|\rho_\lambda\rangle}. \tag{4.13}$$

This is the equation we have to solve, but this is not suitable for computation, since both numerators and denominators in left and right hand sides in Eq. (4.13) contain divergent terms. These divergences have to be removed to obtain a meaningful equation. This should be done by use of the decomposition theorem [29, 30, 32]. The diagrams $U(0,-\infty)|\Phi_\alpha\rangle$ can actually be factorized as bellow

$$\begin{aligned} U(0,-\infty)|\Phi_\alpha\rangle = {} & \langle U\rangle\times U_Q(0,-\infty)|c\rangle \\ & \times\sum_{\beta=1}^{d}U_{VQ}(0,-\infty)|\Phi_\beta\rangle\langle\Phi_\beta|U_V(0,-\infty)|\Phi_\alpha\rangle, \end{aligned} \tag{4.14}$$

[*1] The time-development operator here is defined in the interaction picture. The subscript I, which is usually used, is omitted.

[*2] One can also write $U(0,-\infty)$ with time-ordering operator, but in folded diagram theory Eq. (4.12) is used.

where $\langle U\rangle = \langle c|U(0,-\infty)|c\rangle$. The subscript V means that all the vertices are linked to at least one valence line, and the Q implies that all wave functions, except for the non-interacting term, are in the excluded state at $t=0$. This is actually the final result of the decomposition theorem, and the details are written in the text books [29, 30, 31]. Note that both $\langle U\rangle$ and $\langle\Phi_\beta|U_V|\Phi_\alpha\rangle$ are divergent since they contain terms which have zero energy denominators. The theory therefore is constructed so that these terms cancel away. Substitution of Eq. (4.14) into the numerators in Eq. (4.13) yields

$$\sum_{\alpha=1}^{d} H\Omega_V(0,-\infty)|\Phi_\alpha\rangle b_\alpha^{(\lambda)} = \sum_{\beta=1}^{d} E_\lambda \Omega_V(0,-\infty)|\Phi_\beta\rangle b_\beta^{(\lambda)}, \tag{4.15}$$

where $b_\alpha^{(\lambda)}$ and Ω_V are defined as

$$b_\alpha^{(\lambda)} \equiv \sum_{i=1}^{d} C_i^{(\lambda)} \frac{\langle\Phi_\alpha|U_V(0,-\infty)|\Phi_i\rangle}{\langle\rho_\lambda|U(0,-\infty)|\rho_\lambda\rangle}\langle U\rangle = \frac{\langle\Phi_\alpha|\Psi_\lambda\rangle}{\langle\rho_\lambda|\Psi_\lambda\rangle}, \tag{4.16}$$

$$\Omega_V(0,-\infty)|\Phi_i\rangle = U_{VQ}(0,-\infty)|\Phi_i\rangle \times U_Q(0,-\infty)|c\rangle. \tag{4.17}$$

One can see that $b_\alpha^{(\lambda)}$ is actually proportional to the projection of the true eigenstate onto the model-space. Recalling the fact that, among $\Omega_V(0,-\infty)|\Phi_i\rangle$, only the non-interacting term is in the model-space at $t=0$,

$$\langle\Phi_\alpha|\Omega_V(0,-\infty)|\Phi_\beta\rangle = \delta_{\alpha\beta}. \tag{4.18}$$

Thus, multiplying Eq. (4.15) with the model-space basis state $\langle\Phi_\gamma|$,

$$\sum_{\alpha=1}^{d}\langle\Phi_\gamma|H_{\rm eff}|\Phi_\alpha\rangle b_\alpha^{(\lambda)} = E_\lambda b_\gamma^{(\lambda)}, \qquad H_{\rm eff} = H\Omega_V(0,-\infty). \tag{4.19}$$

Defining the vector

$$|b_\lambda\rangle = \sum_{k=1}^{d} b_k^{(\lambda)}|\Phi_k\rangle, \tag{4.20}$$

one can express Eqs. (4.19), (4.16) in a compact form

$$PH_{\rm eff}P|b_\lambda\rangle = E_\lambda|b_\lambda\rangle, \qquad |b_\lambda\rangle = \frac{P|\Psi_\lambda\rangle}{\langle\rho_\lambda|\Psi_\lambda\rangle}. \tag{4.21}$$

This is the model-space secular equation of dimension d[*3]. In order to remove the core contribution from Eq. (4.19), we decompose interaction term of the Hamiltonian H_1 into $H_1(C)$ which gives rise to diagrams in which H_1 is not linked to any valence line at time $t = 0$ and the valence part $H_1(V)$ which contains all the other diagrams. Thus, the latter contributions lead to the two-body part of the true core energy E_C[*4]. Since $|\Phi_i\rangle$ are the eigenstates of H_0,

$$\begin{aligned}\langle\Phi_i|H\Omega_V(0,-\infty)|\Phi_j\rangle &= \langle\Phi_i|H_0|\Phi_j\rangle + \langle\Phi_i|(H_1(V)+H_1(C))\Omega_V(0,-\infty)|\Phi_j\rangle \\ &= \delta_{ij}(\epsilon_V+\epsilon_C) + \langle\Phi_i|H_1(V)\Omega_V(0,-\infty)|\Phi_j\rangle + E_C - \epsilon_C. \end{aligned} \tag{4.22}$$

Using this in Eq. (4.19), we obtain

$$\sum_{i=1}^{d}\langle\Phi_k|H_0(V)+H_1(V)\Omega_V(0,-\infty)|\Phi_i\rangle b_k^{(\lambda)} = (E_\lambda - E_C)b_k^{(\lambda)}. \tag{4.23}$$

This is nothing but the model-space eigenvalue problem where the core energy is successfully separated. Then we can rewrite Eq. (4.23) as

$$\sum_{i=1}^{d}\langle\Phi_k|H_0(V)+V_{\text{eff}}|\Phi_i\rangle b_k^{(\lambda)} = (E_\lambda - E_C)b_k^{(\lambda)}, \tag{4.24}$$

where

$$\langle\Phi_i|V_{\text{eff}}|\Phi_j\rangle = \langle\Phi_i|H_1(V)\Omega_V(0,-\infty)|\Phi_j\rangle \tag{4.25}$$

is the effective interaction. The structure of the effective interaction can be written as

$$V_{\text{eff}} = \hat{Q} - \hat{Q}'\int\hat{Q} + \hat{Q}'\int\hat{Q}\int\hat{Q} - \cdots. \tag{4.26}$$

Here, $\hat{Q}$ is called Q-box which is the sum of all the diagrams that have at least one H_1-vertex and are irreducible (i.e. contain at least one passive line(Q-space state) between

[*3]One have to note that $|b_\lambda\rangle$ are not orthogonal, i.e. $\langle b_\lambda|b_\mu\rangle \neq \delta_{\lambda\mu}$, since the projection of orthogonal vectors onto a smaller space does not generally result in orthogonal projected vectors. Thus, H_{eff} is not necessarily hermitian. This problem can be overcome by defining vectors $|\bar{b}_\lambda\rangle$ in the model-space which are bi-orthogonal to $|b_\lambda\rangle$.

[*4]This is due to the Goldstone theorem. The contributions $\langle\Phi_i|H_1(C)U_{VQ}|\Phi_j\rangle U_Q|c\rangle = \delta_{ij}\langle c|H_1(c)U_Q|c\rangle$ are the summation of all the linked diagrams. This is nothing but the ground state of a closed-shell system.

two successive vertices) and valence-linked (i.e. have all the vertices linked to at least one valence line). $\hat{Q}'$ is at least second order in the interaction H_1, while $\hat{Q}$ starts with first order terms. The $\int$ signs represent the folding operation[*5] and this operation can be described in terms of the energy derivative of $\hat{Q}$-box, like

$$-\hat{Q}' \int \hat{Q} = \frac{d\hat{Q}(\omega)}{d\omega}\hat{Q}(\omega), \tag{4.27}$$

where ω is a starting energy, that is, the sum of the energies of incoming particles. The general expression for an n-folded $\hat{Q}$-box is

$$\hat{Q} - \hat{Q}' \int \hat{Q} + \hat{Q}' \int \hat{Q} \int \hat{Q} - \cdots = \sum_{k_1 \cdots k_n} \frac{1}{k_1!}\frac{d^{k_1}\hat{Q}'}{d\omega^{k_1}} P \frac{1}{k_2!}\frac{d^{k_2}\hat{Q}}{d\omega^{k_2}} P \cdots \frac{1}{k_n!}\frac{d^{k_n}\hat{Q}}{d\omega^{k_n}} P\hat{Q}, \tag{4.28}$$

under the constrain

$$k_1 + \cdots k_n = n, \quad k_1 \geq 1, \quad k_l \leq n - l + 1. \tag{4.29}$$

One possible solution can be obtained by the iteration

$$V_{\text{eff}}^{(n)} = \hat{Q} + \sum_{k=1}^{\infty} \frac{1}{k!}\frac{d^k\hat{Q}'}{d\omega^k}\left\{V_{\text{eff}}^{(n-1)}\right\}^k, \qquad V_{\text{eff}}^{(0)} = \hat{Q}. \tag{4.30}$$

This expansion is used in our calculations.

4.2 Realistic nucleon-nucleon interaction

Since QCD is commonly believed to describe the theory of the strong interaction, the nucleon-nucleon (NN) interaction V_{NN} may be determined in principle by the underlying quark-quark dynamics in QCD. However, the quantitative understanding of the NN interaction from the QCD have not been fully obtained because of the non-perturbative character of QCD at low energies. This situation has been circumvented by introducing models which contain some of the properties of QCD, such as confinement and chiral symmetry breaking. Among them, boson exchange model and chiral perturbation theory give the most quantitative representation of the NN interaction in the energy regime of

[*5] $\hat{Q}$-boxes and the folding operation are introduced in the context of the decomposition procedure.

nuclear physics. The potentials obtained through the method above are called realistic NN potentials, and these potentials are the starting point of the microscopic theory of the nuclear structure. In many-body perturbation theory discussed in Sect. 4.1, one cannot use the realistic NN interactions, since all of them yield strongly repulsive or diverging matrix elements at short distances. In order to remove these divergences, renormalized NN interactions have been constructed from the Brueckner G-matrix approach [49]. The matrix elements of G in the unperturbed basis are finite. The perturbation expansion for G can be represented by the infinite series of ladder diagrams. The physical interpretation of this is intuitively clear. Since V_{NN} is very strong in the unperturbed basis, the particles must interact virtually with each other an arbitrary number of times so as to produce a finite interaction matrix element. On the other side, an alternative renormalization scheme which integrates out the high momentum components of the realistic nucleon-nucleon interactions has been proposed [50, 51]. Using a similarity transformation of the two-nucleon Hamiltonian[*6], a soft-core effective interaction is obtained in a model-space which is defined by a cutoff Λ in the relative momentum between the nucleons. This renormalized interaction is known as a low-momentum nucleon-nucleon interaction or $V_{\text{low-k}}$. $V_{\text{low-k}}$ does not depend on energy and nucleus and can reproduce nucleon-nucleon scattering data, but has a sizable dependence on Λ. One can perform the many-body perturbation in terms of these renormalized interactions and can obtain the effective interaction for the shell model. This prescription has a long history and many calculations have been done using G-matrix obtained from several NN potentials. Unfortunately, the agreement between the calculated and experimental spectra is not perfect. As for the drip line oxygen isotopes, the drip line property has not been reproduced with G-matrix in *sd*-space.

[*6] Or one can construct the low-momentum effective interaction from the condition that in the low-momentum model space a $V_{\text{low-k}}$ reproduces the original T-matrix which is derived from a NN interaction.

4.3 Shell-model calculations using effective interactions derived from the realistic nucleon-nucleon interaction

In this section, we show some results of shell-model calculations using the effective interactions which are microscopically derived through many-body perturbation theory. Since the main purpose of this thesis is to discuss about the continuum effects, perturbation with continuum basis (the basis obtained in Sect. 2.1 or alternative one) might be the best to construct the effective interactions for shell model. Unfortunately that may be the future work, so in the first step, we check how much our effective interactions work well for the drip-line oxygen isotopes. We adopt N^{3}LO potential [52, 53] as a realistic nucleon-nucleon interaction, and renormalize it into $V_{\text{low-k}}$ or G-matrix. Then we perform the perturbation in terms of these interactions so as to obtain the effective interaction for $(1s_{1/2}0d_{3/2})$ or full *sd*-space. As for the one-body part of the effective Hamiltonian, single-particle energies are fitted to the experimental energy differences. Calculations are done using the code constructed by M.H.Jensen[*7]. We show a part of the results in Figs. 4.2 and 4.3 where the difference between these two figures is the model space. In Fig. 4.2, the results of calculations in *sd*-space are shown. Fig. 4.2(a) corresponds to the result from $V_{\text{low-k}}$. In the computation of $\hat{Q}$-boxes, intermediate states are truncated by the value $n_{\max}$ and $l_{\max}$, which are the principle quantum number and the orbital angular momentum of the single-particle states in the laboratory system, respectively. Considering the diagram in Fig. 4.1 as an example, intermediate states denoted by p and h are summed over. The summation over h is finite since there are only three orbits for h in the ^{16}O core, that is $0s_{1/2}, 0p_{3/2}$ and $0p_{1/2}$. The summation over p however is infinite, including all the single-particle orbits from $0d_{5/2}$. This summation is truncated at $(2n_{\max} + l_{\max})\hbar\omega$, which means the particle-hole excitation is restricted as $\epsilon_p - \epsilon_h \leq (2n_{\max} + l_{\max})\hbar\omega$. Since the contributions from the higher $d_{3/2}$ orbit can be important for the oxygen isotopes near the drip line, we change the value of $n_{\max}$ as $n_{\max} = 1, \cdots, 9$. For $n_{\max} \geq 3$, the results are not so changed. One can see that effective interactions for the full *sd*-space cannot reproduce the experimental

[*7] Morten Hjorth-Jensen, University of Oslo.

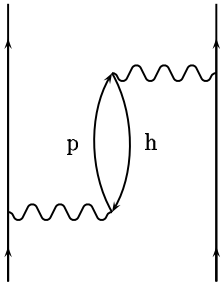

Figure 4.1: An example of $\hat{Q}$-box diagrams.

tendency in drip-line oxygen isotopes. The $3/2^+$ state in ^{25}O and the 0^+ and 2^+ states in ^{26}O are both calculated to be bound states, which contradicts the fact that ^{24}O is the last nucleus where the ground state can exist as a bound state. Beside that, one neutron separation energy of ^{24}O is much lager ($\sim$ 6 MeV) than experimental data [54] in which $S_n \sim 4$MeV. Furthermore, $3/2^+$ state in ^{23}O and $1^+, 2^+$ states in ^{24}O are all calculated to be bound states. This does not agree with the experiments [47, 40]. The situation does not change when G-matrix is used in stead of $V_{\text{low-k}}$ as shown in Fig. 4.2(b). This has actually been the well known problem [55, 35], and a motivation of adopting phenomenological effective interaction as discussed in Ref. [42]. One should note that although V_{eff} derived in Sect. 4.1 is formally exact, actual calculations can only be approximate. First, there is no assurance that the order-by-order perturbations converge. Second, harmonic oscillator basis used for the calculations of vertices and energy denominators in each $\hat{Q}$-box is an approximation. Beside these two points, real three-body forces are missed in the current perturbation theory.

We perform the same procedure for $(1s_{1/2}0d_{3/2})$ space. Using $V_{\text{low-k}}$ interaction which is deduced from N^{3}LO potential, $\hat{Q}$-box expansion is performed, taking $(1s_{1/2}0d_{3/2})$ shell as the P-space. If we take the $(1s_{1/2}0d_{3/2})$ space, the drip-line properties are reproduced as in Fig. 4.3. The essential difference between phenomenological effective interactions which can rather well reproduce the experimental spectra and the effective interaction derived using G-matrix might be understood by comparing their monopole terms, which are defined in Eq. (3.10). Looking at Tab. 4.1, one can clearly see that the monopole terms

	$V^{T=1}_{0d5/2,0d3/2}$	$V^{T=1}_{0d5/2,1s1/2}$	$V^{T=1}_{0d3/2,1s1/2}$
SDPF-M	-0.01	0.10	-0.03
G-matrix(N^3LO)	-0.64	-0.42	-0.05

Table 4.1: Monopole terms of the orbits in *sd*-shell. All the numbers are written in the unit of MeV.

of G-matrix are strongly attractive compared to those of SDPF-M as long as $0d_{5/2}$ orbit is concerned. Because of this, G-matrix cannot reproduce the experimental tendencies including the $N = 14$ shell gap. The monopole terms between $0d_{3/2}$ and $1s_{1/2}$ orbits, on the other hand, are not so different. Hence, if we assume six neutrons in $0d_{5/2}$ orbit as an inert core, then we can obtain, using the G-matrix, the spectra similar to that from the phenomenological interaction (SDPF-M).

We show in Fig. 4.3 the results with $(1s_{1/2}, 0d_{3/2})$ space. The difference between these three is the order of H_1 in $\hat{Q}$-boxes diagrams. Since folded diagrams appear from the third order in terms of H_1, folded diagrams are not included in Fig. 4.3(a).

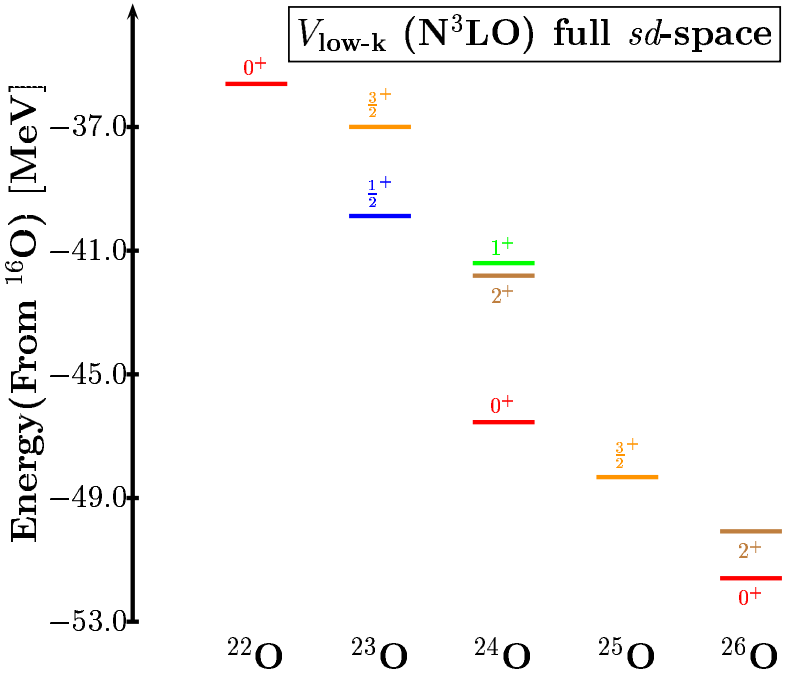

(a) $V_{\text{low-k}}$ case. Q-space is defined by the value $l_{max} = 4, n_{max} = 9$. $\hat{Q}^{(2)}$ +folded diagrams.

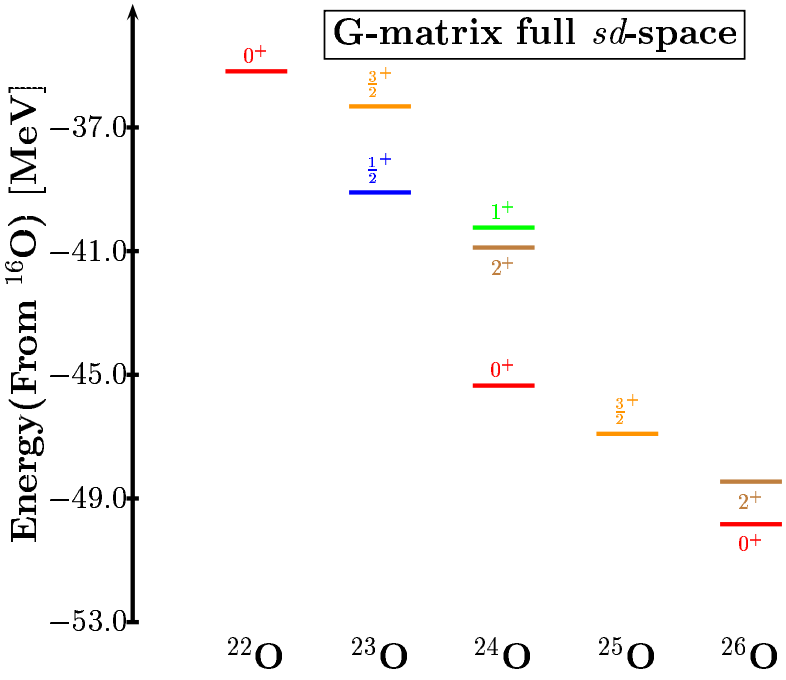

(b) G-matrix case. Q-space is defined by the value $l_{max} = 7, n_{max} = 3$. $\hat{Q}^{(3)}$ +folded diagrams.

Figure 4.2: Shell-model calculation of the spectra in drip line oxygen isotopes. The effective interaction is designed for full *sd*-space.

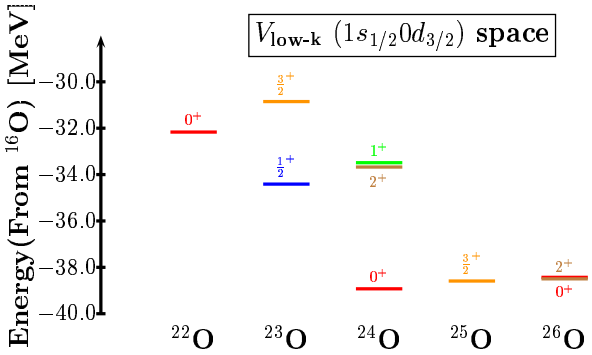

(a) $V_{\text{low-k}}$ case. Q-space is defined by the value $l_{max} = 4, n_{max} = 9$, $\hat{Q}^{(1)}$.

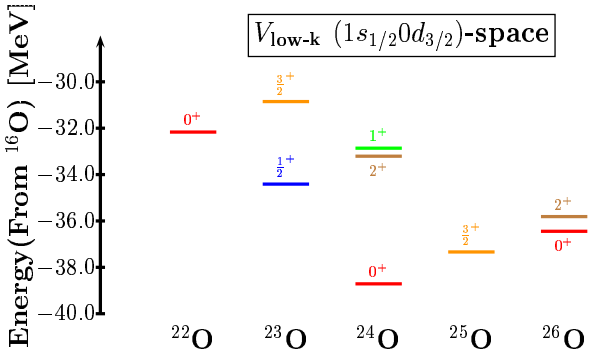

(b) $V_{\text{low-k}}$ case. Q-space is defined by the value $l_{max} = 4, n_{max} = 9$, $\hat{Q}^{(2)}$ +folded diagrams

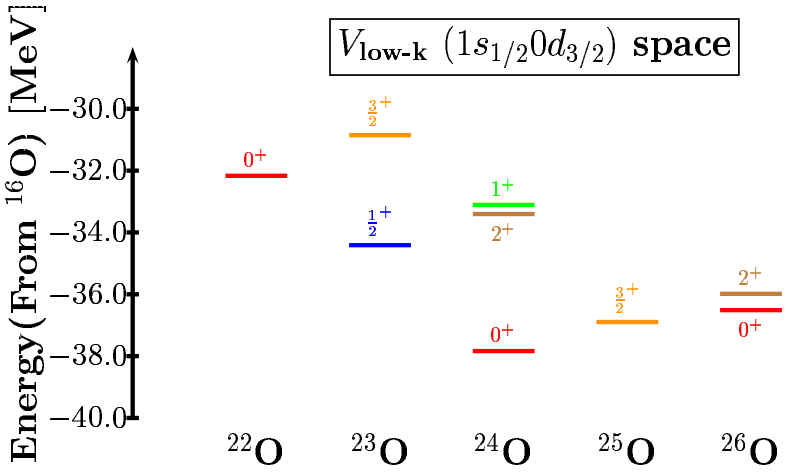

(c) $V_{\text{low-k}}$ case. Q-space is defined by the value $l_{max} = 4, n_{max} = 9$, $\hat{Q}^{(3)}$ +folded diagrams

Figure 4.3: Shell-model calculation of the spectra in drip line oxygen isotopes. The effective interaction is designed for $(s_{1/2}0d_{3/2})$ space. $\hat{Q}^{(k)}$ means each $\hat{Q}$-box is calculated up to kth oder in terms of H_1.

4.4 Application to the shell-model calculation with the continuum basis

Since the effective interactions deduced from the realistic nucleon-nucleon interactions have been obtained, one can use these matrix elements to determine the Hamiltonian of the continuum shell model discussed in Sect. 2. To be specific, we can determine the parameters g_i, a_i in Eq. (2.4d) so that the matrix elements of the interaction in Eq. (2.4d) become close enough to those of the effective interaction derived in Sect. 4.1. We choose the effective interaction obtained through perturbation in terms of $V_{\text{low-k}}$ into which N^{3}LO potential is renormalized. Then we get

$$g_1 = -5.0, \quad g_2 = 20, \quad a_1 = -0.4, \quad a_2 = 1.6\ . \tag{4.31}$$

Since we have no information about the single-particle energies in this space, we take the experimental energy differences,

$$\tilde{\epsilon}_{0d3/2} = E(3/2^+;^{23}\text{O}) - E(\text{g.s.};^{22}\text{O}), \quad \tilde{\epsilon}_{1s1/2} \quad = E(1/2^+;^{23}\text{O}) - E(\text{g.s.};^{22}\text{O}), \tag{4.32}$$

then the strength of Woods-Saxon potential to generate the continuum basis is determined on the condition that the threshold energy of $3/2^+$ state in ^{23}O should be equal to $\tilde{\epsilon}_{0d3/2}$.

	^{23}O	^{24}O		^{25}O	^{26}O	
States	$3/2^+$	1^+	2^+	$3/2^+$	0^+	2^+
V_{low-k}	1.26	1.30	1.01	0.94	1.32	1.85
V_{low-k}(with continuum)	1.26	1.26	0.98	0.93	**0.65**	**1.1**
Experiments	1.26	1.35	0.66	0.77	-	-

Table 4.2: The threshold energies of low-lying states in O isotopes near the drip line.

Final results are shown in Tab. 4.2. Even at the level of bound approximation, the experimental tendencies are well described, however the continuum effects can be seen in ^{26}O. The reason why the difference between the cases with and without continuum effects is so small can be thought that the strengths of the effective interaction in Eq. (4.31) are very small.

Chapter 5

Summary and perspective

In this thesis, we mainly have investigated the continuum effects for the low-lying states in oxygen isotopes near the neutron drip line. In this unstable region, many unbound states start from low excitation energies. Thus the coupling with the continuum states can be important and should be evaluated. In Chapter 2, we set up our method. The neutron $0d_{3/2}$ orbit in drip-line oxygen isotopes is pushed up due to the nuclear force, and its single-particle energy becomes zero or positive. In such a case, it is not sufficient to describe this single-particle state by the conventional harmonic oscillator functions. Thus a continuum basis is generated by solving the spherical one-body Schrödinger equation with the boundary condition that the wave function should be zero at a large distance, $L = 1000$ fm. Then we assume the phenomenological central force for the two-body part of the Hamiltonian. The parameters are determined so that the matrix elements of our effective interaction reproduce those of the ordinary shell-model effective interactions which can be either phenomenological one (SDPF-M) or one deduced by a realistic nucleon-nucleon interaction. Ideally, the calculations should be performed in *sd*-space, considering the configuration-mixing effect. However, in order to reduce the dimension of the Hamiltonian matrix, we take $(1s_{1/2}0d_{3/2})$ space.

In Chapter 3, we performed the shell-model calculation with and without the continuum effects for $^{23-26}$O. In the case of ^{23}O, since there is one valence neutron in the model space, $3/2^+$ state in ^{23}O is obtained as the one-neutron resonance for ^{22}O core. Due to the coupling with the continuum $d_{3/2}$ states, the peak of this resonance state is located about

1 MeV below the single-particle energy of $0d_{3/2}$ orbit in ordinary shell model, and get close to the experimental value. The 1^+ and 2^+ states in ^{24}O are pushed up and down from the resonance, respectively. This is caused by the residual interaction, and the effects are about 0.4 MeV in energy. These states have a good agreement with those obtained by experiments. Since the neutron $1s_{1/2}$ orbit is occupied in ^{25}O, two-body matrix elements in $(1s_{1/2}id_{3/2})$ space are written in terms of monopole terms between $1s_{1/2}$ and $id_{3/2}$ orbits. As discussed in Sect. 3.3, these monopole terms are small ($\sim$ 0.1 MeV) compared to the matrix elements themselves, therefore the threshold energy of the $3/2^+$ state in ^{25}O is very close to the resonance. Also our calculation can reproduce the experimental data. As for ^{26}O, the coupling with the continuum states lowers the 0^+ and 2^+ states by 2.8 MeV and 2.7 MeV, respectively. These states are calculated to be unbound states. This is consistent with the experiments. Radial distributions of the neutrons in continuum $d_{3/2}$ orbits are also obtained for each isotope. They are generally similar to the density distribution of the one-neutron resonance inside the nucleus and gradually approach the spherical Bessel function of the corresponding k value far outside the nuclei. With the residual interaction, each wave function actually changes from that of the resonance in and near the nuclear surface.

As a whole, our calculations provide good results. When one considers SDPF-M interaction, the model-space dependences of the shell-model calculations are rather small, and the coupling with the continuum $d_{3/2}$ orbits is essential for low-lying states in drip-line oxygen isotopes.

In Chapter 4, the focus is towards the microscopic derivation of the effective interaction $V_{\rm eff}$ for the shell-model calculation. As for the derivation of $V_{\rm eff}$ in general, one approach is to parameterize $V_{\rm eff}$ with adjustable parameters based on a starting point provided by a microscopic theory. The remarkably good results obtained with shell model indicate the general validity of the effective interaction approach, indicating the existence of such a $V_{\rm eff}$. The alternative approach is to derive $V_{\rm eff}$ from the first principle. These two approaches are complementary to each other. In Sects. 4.1 and 4.2, the brief outline of this method is shown. The procedure consists of two steps. First, a realistic nucleon-nucleon interaction is renormalized into G-matrix or $V_{\rm low\text{-}k}$ in order to remove the divergence of the matrix elements at short inter-nucleonic distances. Then the effective interaction in a model space

is obtained through many-body perturbation theory, that is, $\hat{Q}$-box expansion. We derive the effective interactions for *sd*-shell from N^{3}LO potential, considering ^{18}O, which has two valence neutrons. So $V_{\rm eff}$ has only 1- and 2-body components. Then we use this two-body components for the shell-model calculations of all the oxygen isotopes near drip line. As for the one-body components, we take the experimental energy differences between ^{23}O and ^{22}O.

As already known, our $V_{\rm eff}$ in *sd*-space cannot reproduce the experimental tendency at all. The cause of this disagreement might be the strongly attractive monopole terms containing $0d_{5/2}$ orbit. Starting from $(1s_{1/2}0d_{3/2})$ space, we temporarily circumvent this problem and $V_{\rm eff}$ in this space can reproduce the experimental tendency. Moreover we apply this $V_{\rm eff}$ to the shell-model calculation with continuum $d_{3/2}$ orbits. In this case, we adjust the one particle resonance for ^{22}O core to the threshold energy of $3/2^+$ in ^{23}O obtained by experiment. The differences between the results with and without continuum effects are very small ($\sim 10^{-2}$ MeV) except that in ^{26}O, where both 0^+ and 2^+ states are lowered by about 0.7 MeV from those of the bound approximation. Anyway both calculations can well describe the experimental data.

We have shown the importance of the continuum single-particle states especially from the resonance. The remaining problem is that $V_{\rm eff}$ derived from a realistic nucleon-nucleon potential does not work well in this mass region. We should note however that $V_{\rm eff}$ is computed using harmonic oscillator wave functions as single-particle states. One may therefore be able to improve $V_{\rm eff}$, by using a basis which consists of both bound and continuum states. Using the modified $V_{\rm eff}$, we may be able to perform the systematic and microscopic calculation towards the exotic nuclei. In doing this, the construction of the single-particle basis must be crucial. One of the efficient methods is the contour deformation method (CDM) [56]. With CDM, we can construct the so-called Berggren basis which can contain bound, antibound, resonance and the non-resonant scattering states. Furthermore, the boundary condition is automatically satisfied. Thus, we can obtain the $V_{\rm eff}$ which has a lot of information about continuum properties by performing $\hat{Q}$-box expansion using the Berggren basis. This would be a future work.

Acknowledgments

I would like to express gratitude to my supervisor Professor Takaharu Otsuka for stimulating discussions and challenging assignment during my work in master course. I'm also thankful towards Assistant Professor Noritaka Shimizu for giving me thorough training in computational techniques and in-depth guidance. I also very grateful to Doctor Yutaka Utsuno for many advises and guidances during the stay in Japan Atomic Energy Agency (JAEA).

Also, I would like to thank Center of Mathematics for Applications (CMA) at the University of Oslo for letting me stay there for a month in November 2007. I'm especially thankful towards Professor Morten Hjorth-Jensen for giving me excellent guidances and arranging a great environment for me during the stay in Oslo. Finally I would like to thank all my friends for giving me support and stimulating discussions over the last two years.

Appendix A

matrix elements of two-body interaction

The matrix elements of two-body interactions are necessary for the phenomenological analysis in nuclear physics. Two-body interactions can be easily expanded into series of tensor products of spherical harmonics by considering Fourier transforms. Then the matrix elements can be obtained by using the method of tensor operators. The procedure will be shown in this section, according to Ref.[39].

A.1 The methods of tensor operator

The spatial part of a two-body interaction is taken to be $V(\boldsymbol{r}) = V(r)C^{(\kappa)}(\Omega)$, where $r = |\boldsymbol{r}| = |\boldsymbol{r}_1 - \boldsymbol{r}_2|$, and Ω denotes the direction of the vector $\boldsymbol{r}$.

$$C_q^{(\kappa)}(\Omega) \equiv \sqrt{\frac{4\pi}{2k+1}} Y_q^{(\kappa)}(\Omega) \tag{A.1}$$

are the unnormalized spherical harmonics. Two-body interactions $V(\boldsymbol{r})$ can be expanded in terms of tensor products of the spherical harmonics,

$$\begin{aligned} V(\boldsymbol{r}) = V(r)C^{(\kappa)}(\Omega) = \sum_{k_1,k_2} i^{k_1-k_2+\kappa} \frac{(2k_1+1)(2k_2+1)}{2\kappa+1} (k_1 0 k_2 0|\kappa 0) \\ \times \left[C^{(k_1)}(\Omega_1) \times C^{(k_2)}(\Omega_2)\right]^{(\kappa)} v^{(k_1,k_2;\kappa)}(r_1, r_2), \end{aligned} \tag{A.2}$$

where $v^{(k_1,k_2;\kappa)}(r_1,r_2)$ are written as

$$v^{(k_1,k_2;\kappa)}(r_1,r_2) = \int_0^\infty dpp^2 j_{k_1}(pr_1) j_{k_2}(pr_2) v_\kappa(p), \tag{A.3}$$

and

$$v_\kappa(p) = \frac{2}{\pi}\int_0^\infty drr^2 V(r) j_\kappa(pr). \tag{A.4}$$

$j_\kappa(z)$ are the spherical Bessel function. If κ equals to zero, the interaction is central, and if $\kappa = 2$, the interaction is tensor.

In the case of the central interaction, where $\kappa = 0$ and $C^{(0)}(\Omega) = 1$, Eq. (A.2) becomes simple, by putting $k_1 = k_2 = k$, as

$$V(r) = 4\pi \sum_k v^{(k)}(r_1,r_2)\left(Y^{(k)}(\Omega_1)\cdot Y^{(k)}(\Omega_2)\right), \tag{A.5}$$

where $v^{(k)}(r_1,r_2) \equiv v^{(k,k;0)}(r_1,r_2)$. Using Eq. (A.5), matrix elements are calculated by the method of tensor operators[38] as

$$\begin{aligned}
\langle a_1a_2|V(r)|a_3a_4\rangle_{JT} &= N_{12}N_{34}\left[\langle a_1a_2|V|a_3a_4\rangle^p_{JT} - (-1)^{j_1+j_2-J+1-T}\langle a_1a_2|V|a_4a_3\rangle^p_{JT}\right], \\
&\text{where } N_{ij} \equiv \frac{1}{\sqrt{(1+\delta_{a_ia_j})}}. \\
\langle a_1a_2|V(r)|a_3a_4\rangle^p_{JT} &= 4\pi(-1)^{j_2+j_3+J}\sum_{k=0}^\infty \left\{ \begin{array}{ccc} j_1 & j_2 & J \\ j_4 & j_3 & k \end{array} \right\} \left(j_1||Y^{(k)}||j_3\right)\left(j_2||Y^{(k)}||j_4\right) R^{(k)}(a_1a_2;a_3a_4),
\end{aligned} \tag{A.6}$$

where a_i means a set of quantum numbers of single-particle states, and j_i are the corresponding angular momenta. The superscript p indicates that this is the "product" wave function. $R^{(k)}(a_1a_2;a_3a_4)$ are given as

$$R^{(k)}(a_1a_2;a_3a_4) = \int_0^\infty\int_0^\infty dr_1dr_2r_1^2r_2^2\psi_{a_1}(r_1)\psi_{a_2}(r_2)v^{(k)}(r_1,r_2)\psi_{a_3}(r_1)\psi_{a_4}(r_2). \tag{A.7}$$

Similarly, in the case of $\boldsymbol{\sigma}_1 \cdot \boldsymbol{\sigma}_2 V(r)$,

$$\langle a_1 a_2 | \boldsymbol{\sigma}_1 \cdot \boldsymbol{\sigma}_2 V(r) | a_3 a_4 \rangle^p_{JT} = 16\pi(-1)^{j_2+j_3+J} \sum_{k=0}^{\infty} R^{(k)}(a_1 a_2; a_3 a_4) \sum_{r=0}^{\infty} (-1)^{k+r+1} \left\{ \begin{array}{ccc} j_1 & j_2 & J \\ j_4 & j_3 & r \end{array} \right\}$$
$$\times \left(j_1 || [\boldsymbol{s}_1 \times Y_1^{(k)}]^{(r)} || j_3 \right) \left(j_2 || [\boldsymbol{s}_2 \times Y_2^{(k)}]^{(r)} || j_4 \right) \quad \text{(A.8)}$$
$$= 16\pi(-1)^{j_2+j_3+J} \hat{j}_1 \hat{j}_2 \hat{j}_3 \hat{j}_4 \sum_{k=0}^{\infty} R^{(k)}(a_1 a_2; a_3 a_4) \sum_{r=0}^{\infty} (-1)^{k+r+1} (2r+1)$$
$$\times \left\{ \begin{array}{ccc} j_1 & j_2 & J \\ j_4 & j_3 & r \end{array} \right\} \left\{ \begin{array}{ccc} \frac{1}{2} & l_1 & j_1 \\ \frac{1}{2} & l_3 & j_3 \\ 1 & k & r \end{array} \right\} \left\{ \begin{array}{ccc} \frac{1}{2} & l_2 & j_2 \\ \frac{1}{2} & l_4 & j_4 \\ 1 & k & r \end{array} \right\}$$
$$\times \left(\frac{1}{2} \middle|\middle| \boldsymbol{s} \middle|\middle| \frac{1}{2} \right)^2 \left(l_1 || Y^{(k)} || l_3 \right) \left(l_2 || Y^{(k)} || l_4 \right), \quad \text{(A.9)}$$

where $\hat{x} = \sqrt{2x+1}$. The radial integrals $R^{(k)}(a_1 a_2; a_3 a_4)$ are generally difficult to carry out analytically for single-particle wave functions with arbitrary radial dependence.

A.2 Radial integrals

We continuously assume the case of the central interaction. Substituting Eq. (A.3) into (A.7), putting $k_1 = k_2 = k, \kappa = 0$, yields

$$R^{(k)}(a_1 a_2; a_3 a_4) = \int_0^{\infty} dp p^2 v_0(p) I^{(k)}(p; a_1, a_3) I^{(k)}(p; a_2, a_4), \quad \text{(A.10)}$$

where $I^{(k)}(p; a_i, a_j)$ are defined as

$$I^{(k)}(p; a_i, a_j) \equiv \int_0^{\infty} dr r^2 \psi_{a_i}(r) \psi_{a_j}(r) j_k(pr) \quad \text{(A.11)}$$

When harmonic oscillator wave functions

$$\psi_{nl} = \sqrt{\frac{2^{l-n+2}(2\nu)^{l+3/2}(2n+2l+1)!!}{\sqrt{\pi} n! [(2l+1)!!]^2}} r^l e^{-\nu r^2} S_n^{(l)}(2\nu r^2), \quad (n = 0, 1, \cdots) \quad \text{(A.12)}$$

are used, $I^{(k)}(p; nl, n'l')$ and hence the radial integrals can be calculated analytically. Here, $S_n^{(l)}(z)$ are given as

$$S_n^{(l)}(z) = \sum_{\mu} \left(\begin{array}{c} n \\ \mu \end{array} \right) \frac{(2l+1)!!}{(2l+2\nu+1)!!} (-2z)^{\mu}, \quad \mathcal{L}_n^{(l+1/2)}(z) = \frac{(2n+2l+1)!!}{2^n n! (2l+1)!!} S_n^{(l)}(z), \quad \text{(A.13)}$$

where $\mathcal{L}_n^\alpha(z)$ are the associated Laguerre polynomial. $\nu = m\omega/(2\hbar)$, $\hbar\omega$ is energy quantum, and m is mass. It is convenient to introduce the expansion of $S_n^{(l)}$

$$S_n^{(l)}(z)S_n^{\prime(l')}(z) = \frac{(2l+1)!!(2l'+1)!!}{(2l+2n+1)!!(2l'+2n'+1)!!}\sum_{\mu=0}^{n+n'} a_{l+l'+2\mu}(nl,n'l')(2z)^\mu, \tag{A.14}$$

where the coefficients $a_m(nl,n'l')$ are

$$a_{l+l'+2\mu}(nl,n'l') = (-1)^\mu \sum_{(m+m'=\mu)} \begin{pmatrix} n \\ m \end{pmatrix}\begin{pmatrix} n' \\ m' \end{pmatrix}\frac{(2l+2n+1)!!}{(2l+2m+1)!!}\frac{(2l'+2n'+1)!!}{(2l'+2m'+1)!!}. \tag{A.15}$$

Using Eq. (A.14), $I^k(p;nl,n'l')$ are obtained as

$$I^{(k)}(p;nl,n'l') = M(nl,n'l')^{-1/2}\sum_m a_m(nl,n'l')\frac{(m+k+1)!!}{(2k+1)!!}e^{-p^2/(8\nu)}\left(\frac{p^2}{4\nu}\right)^{k/2} S^{(k)}_{(m-k)/2}(p^2/(8\nu)), \tag{A.16}$$

where

$$M(nl,n'l') = 2^{n+n'}n!n'!(2l+2n+1)!!(2l'+2n'+1)!!. \tag{A.17}$$

Again making use of Eq. (A.14), the radial integral, Eq. (A.10), is obtained as

$$\begin{aligned} R^{(k)}(n_1l_1n_2l_2;n_1'l_1'n_2'l_2') &= [M_1M_2]^{-1/2}\sum_{m_1m_2} a_{m_1}(n_1l_1,n_1'l_1')a_{m_2}(n_2l_2,n_2'l_2') \\ &\quad\times\sum_{m=\bar{k}}^{\bar{m}} a_{2m}\left(\frac{m_1-k_1}{2}k_1,\frac{m_2-k_2}{2}k_2\right)J_m, \end{aligned} \tag{A.18}$$

$$J_m = \frac{1}{(4\nu)^m}\int_0^\infty dpp^{2m+2}v_0(p)e^{-p^2/(4\nu)}, \tag{A.19}$$

where $M_i(i=1,2)$ are the abbreviations of $M(n_il_i,n_i'l_i')$. In the case of Gaussian-type interaction used in this thesis, $V(r) = e^{-r^2/r_0^2}$, J_m is readily calculated as

$$\begin{aligned} J_m &= \frac{1}{(4\nu)^m\pi}\int_0^\infty dpp^{2m+1}e^{p^2/(4\nu)}\mathrm{Im}\int_0^\infty drre^{ipr-r^2/r_0^2} \\ &= \frac{r_0^3}{(4\nu)^m 2\sqrt{\pi}}\int_0^\infty dpp^{2m+2}e^{-(1+\nu r_0^2)p^2/(4\nu)} = \frac{(2m+1)!!}{2^m}\lambda^3(1+\lambda^2)^{-(m+3/2)}, \end{aligned} \tag{A.20}$$

where $\lambda \equiv d\sqrt{\nu}$. Eqs. (A.18) and (A.20) are used to determine the parameters in Sect. 2.2. When continuum basis is considered, $I^{(k)}(p;a_i,a_j)$ have to be computed numerically.

References

[1] G. Gamow. The quantum theory of the atom nucleus. *Zeitschrift für Physik*, 51:204–212, 1928. pages 4

[2] G. Breit and E. Wigner. Capture of Slow Neutrons. *Physical Review*, 49(7):519–531, 1936. pages 4

[3] R.G. Newton. *Scattering Theory of Waves and Particles*. Dover Publications, 2002. pages 4

[4] V.I. Kukulin, VM Krasnopol'sky, and J. Horácek. *Theory of resonances: principles and applications*. Kluwer Academic Publishers, 1989. pages 4, 5

[5] Zel'dovich Y.B. On the theory of unstable states. *SOVIET PHYSICS JETP-USSR*, 12:542, 1961. pages 4

[6] Shigeyoshi Aoyama. Theoretical prediction for the ground state of ^{10}he with the method of analytic continuation in the coupling constant. *Phys. Rev. Lett.*, 89(5):052501, Jul 2002. pages 5

[7] J. Aguilar and J. M. Combes. A class of analytic perturbations for one-body schrödinger hamiltonians. *Communications in Mathematical Physics*, 22:269, 1971. pages 5

[8] E. BalslevandJ. M. Combes. Spectral properties of many-body schrödinger operators with dilatation-analytic interactions. *Communications in Mathematical Physics*, 22:280, 1971. pages 5

[9] N. Moiseyev and C. Corcoran. Autoionizing states of H_2 and H_2^- using the complex-scaling method. *Physical Review A*, 20(3):814–817, 1979. pages 5

[10] N. Moiseyev. Quantum theory of resonances: calculating energies, widths and cross-sections by complex scaling. *Physics Reports*, 302(5-6):212–293, 1998. pages 5

[11] S. Aoyama, S. Mukai, K. Kato, and K. Ikeda. Theoretical Predictions of Low-Lying Three-Body Resonance States in He. *Progress of Theoretical Physics*, 94(3):343–352, 1995. pages 5

[12] S. Aoyama, T. Myo, K. Kato, and K. Ikeda. The Complex Scaling Method for Many-Body Resonances and Its Applications to Three-Body Resonances. *Progress of Theoretical Physics*, 116(1):1–35, 2006. pages 5

[13] Takayuki Myo, Kiyoshi Katō, Shigeyoshi Aoyama, and Kiyomi Ikeda. Analysis of ^6he coulomb breakup in the complex scaling method. *Phys. Rev. C*, 63(5):054313, Apr 2001. pages 5

[14] I.R. Afnan. Resonances in few-body systems. *Australian journal of physics*, 44(2-3):201–216, 1991. pages 5

[15] T. Berggren. USE OF RESONANT STATES IN EIGENFUNCTION EXPANSIONS OF SCATTERING AND REACTION AMPLITUDES. *Nuclear Physics A*, 109:265, 1968. pages 5

[16] Patric Lind. Completeness relations and resonant state expansions. *Phys. Rev. C*, 47(5):1903–1920, May 1993. pages 5

[17] N. Michel, W. Nazarewicz, M. Płoszajczak, and K. Bennaceur. Gamow shell model description of neutron-rich nuclei. *Phys. Rev. Lett.*, 89(4):042502, Jul 2002. pages 7

[18] N. Michel, W. Nazarewicz, M. Płoszajczak, and J. Okołowicz. Gamow shell model description of weakly bound nuclei and unbound nuclear states. *Phys. Rev. C*, 67(5):054311, May 2003. pages 7

[19] N. Michel, W. Nazarewicz, and M. Pószajczak. Proton-neutron coupling in the Gamow shell model: The lithium chain. *Physical Review C*, 70(6):64313, 2004. pages 7

[20] N. Michel, W. Nazarewicz, M. Płoszajczak, and J. Rotureau. Antibound states and halo formation in the Gamow shell model. *Physical Review C*, 74(5):54305, 2006. pages 7

[21] G. Hagen, M. Hjorth-Jensen, and N. Michel. Gamow shell model and realistic nucleon-nucleon interactions. *Physical Review C*, 73(6):64307, 2006. pages 7

[22] M. Thoennessen. Reaching the limits of nuclear stability. *Reports on Progress in Physics*, 67(7):1187–1232, 2004. pages 7

[23] M. Langevin et al. Production of neutron-rich nuclei at the limits of particles stability by fragmentation of 44 mev/u 40ar projectiles. *Physics letters. Section B*, 150:71, 1985. pages 7

[24] M. Thoennessen, T. Baumann, B. A. Brown, J. Enders, N. Frank, P. G. Hansen, P. Heckman, B. A. Luther, J. Seitz, A. Stolz, and E. Tryggestad. Single proton knock-out reactions from ^{24,25,26}F. *Phys. Rev. C*, 68(4):044318, Oct 2003. pages 7

[25] D. Guillemaud-Mueller, J. C. Jacmart, E. Kashy, A. Latimier, A. C. Mueller, F. Pougheon, A. Richard, Yu. E. Penionzhkevich, A. G. Artuhk, A. V. Belozyorov, S. M. Lukyanov, R. Anne, P. Bricault, C. Détraz, M. Lewitowicz, Y. Zhang, Yu. S. Lyutostansky, M. V. Zverev, D. Bazin, and W. D. Schmidt-Ott. Particle stability of the isotopes ^{26}o and ^{32}ne in the reaction 44 mev/nucleon ^{48}ca+ta. *Phys. Rev. C*, 41(3):937–941, Mar 1990. pages 7

[26] M. Fauerbach, D. J. Morrissey, W. Benenson, B. A. Brown, M. Hellström, J. H. Kelley, R. A. Kryger, R. Pfaff, C. F. Powell, and B. M. Sherrill. New search for ^{26}o. *Phys. Rev. C*, 53(2):647–651, Feb 1996. pages 7

[27] H. Sakurai, S.M. Lukyanov, M. Notani, N. Aoi, D. Beaumel, N. Fukuda, M. Hirai, E. Ideguchi, N. Imai, M. Ishihara, et al. Evidence for particle stability of ^{31}F and

particle instability of ^{25}N and ^{28}O. *Physics Letters B*, 448(3-4):180–184, 1999. pages 7

[28] O. Tarasov, R. Allatt, JC Angélique, R. Anne, C. Borcea, Z. Dlouhy, C. Donzaud, S. Grévy, D. Guillemaud-Mueller, M. Lewitowicz, et al. Search for ^{28}O and study of neutron-rich nuclei near the N= 20 shell closure. *Physics Letters B*, 409(1-4):64–70, 1997. pages 7

[29] T.T.S. Kuo. in topics in nuclear physics. *Lecture notes in physics*, 144:248, 1981. pages 12, 34, 35

[30] T.T.S.Kuo Evind Osnes. Folded-diagram theory of the effective interaction in nuclei, atoms and molecules. *Lecture notes in physics*, 364:1, 1990. pages 12, 34, 35

[31] P. J. Ellis and E. Osnes. An introductory guide to effective operators in nuclei. *Rev. Mod. Phys.*, 49(4):777–832, Oct 1977. pages 12, 35

[32] T. Morita. Perturbation Theory for Degenerate Problems of Many-Fermion Systems. *Progress of Theoretical Physics*, 29(3):351–369, 1963. pages 12, 34

[33] C. L. Kung, T. T. S. Kuo, and K. F. Ratcliff. Converged values of second-order core-polarization diagrams with orthogonalized-plane-wave intermediate states. *Phys. Rev. C*, 19(3):1063–1082, Mar 1979. pages 12

[34] Yutaka Utsuno, Takaharu Otsuka, Takahiro Mizusaki, and Michio Honma. Varying shell gap and deformation in $n \sim 20$ unstable nuclei studied by the monte carlo shell model. *Phys. Rev. C*, 60(5):054315, Oct 1999. pages 12

[35] B.A. Brown and B.H. Wildenthal. Status of the nuclear shell model. *Annual Review of Nuclear and Particle Science*, 38(1):29–66, 1988. pages 13, 40

[36] G. Audi and AH Wapstra. The 1995 update to the atomic mass evaluation. *Nuclear Physics A*, 595(4):409–480, 1995. pages 13

[37] E. Sauvan, F. Carstoiu, N.A. Orr, J.C. Angélique, W.N. Catford, N.M. Clarke, M. Mac Cormick, N. Curtis, M. Freer, S. Grévy, et al. One-neutron removal reac-

tions on neutron-rich psd-shell nuclei. *Physics Letters B*, 491(1-2):1–7, 2000. pages 13

[38] I. Talmi. *Simple Models of Complex Nuclei: The Shell Model and Interacting Boson Model*. Harwood Academic Pub, 1993. pages 14, 52

[39] H. Horie and K. Sasaki. On Energy Matrices for the Independent Particle Model. *Progress of Theoretical Physics*, 25(3):475–492, 1961. pages 14, 51

[40] C. Hoffman et al. Determination of the n=16 shell closure at the oxygen drip line. pages 18, 20, 24, 40

[41] M. Stanoiu, F. Azaiez, Z. Dombrádi, O. Sorlin, B.A. Brown, M. Belleguic, D. Sohler, M.G. Saint Laurent, M.J. Lopez-Jimenez, Y.E. Penionzhkevich, et al. N= 14 and 16 shell gaps in neutron-rich oxygen isotopes. *Physical Review C*, 69(3):34312, 2004. pages 20

[42] B.A. Brown and W.A. Richter. New "USD" Hamiltonians for the sd shell. *Physical Review C*, 74(3):34315, 2006. pages 20, 40

[43] M. Wiedeking, S.L. Tabor, J. Pavan, A. Volya, A.L. Aguilar, I.J. Calderin, D.B. Campbell, W.T. Cluff, E. Diffenderfer, J. Fridmann, et al. p-sd Shell Gap Reduction in Neutron-Rich Systems and Cross-Shell Excitations in ^{20} O. *Physical Review Letters*, 94(13):132501, 2005. pages 20

[44] D. Cortina-Gil, J. Fernandez-Vazquez, T. Aumann, T. Baumann, J. Benlliure, M.J.G. Borge, L.V. Chulkov, U. Datta Pramanik, C. Forssén, L.M. Fraile, et al. Shell Structure of the Near-Dripline Nucleus ^{23} O. *Physical Review Letters*, 93(6):62501, 2004. pages 20, 21

[45] H. Savajols, B. Jurado, W. Mittig, D. Baiborodin, W. Catford, M. Chartier, C.E. Demonchy, Z. Dlouhy, A. Gillibert, L. Giot, et al. New mass measurements at the neutron drip-line. *The European Physical Journal A-Hadrons and Nuclei*, 25:23–26, 2005. pages 20

[46] C. Nociforo, K.L. Jones, L.H. Khiem, P. Adrich, T. Aumann, B.V. Carlson, D. Cortina-Gil, U. Datta Pramanik, T.W. Elze, H. Emling, et al. Coulomb breakup of ^{23}O. *Physics Letters B*, 605(1-2):79–86, 2005. pages 21

[47] Z. Elekes, Z. Dombrádi, N. Aoi, S. Bishop, Z. Fülöp, J. Gibelin, T. Gomi, Y. Hashimoto, N. Imai, N. Iwasa, et al. Spectroscopic Study of Neutron Shell Closures via Nucleon Transfer in the Near-Dripline Nucleus ^{23}O. *Physical Review Letters*, 98(10):102502, 2007. pages 21, 40

[48] G. F. Bertsch, P. F. Bortignon, and R. A. Broglia. Damping of nuclear excitations. *Rev. Mod. Phys.*, 55(1):287–314, Jan 1983. pages 25

[49] M. Hjorth-Jensen, T.T.S. Kuo, and E. Osnes. Realistic effective interactions for nuclear systems. *Physics Reports*, 261(3):125–270, 1995. pages 38

[50] S.K. Bogner, T.T.S. Kuo, and A. Schwenk. Model-independent low momentum nucleon interaction from phase shift equivalence. *Arxiv preprint nucl-th/0305035*, 2003. pages 38

[51] S. Fujii, E. Epelbaum, H. Kamada, R. Okamoto, K. Suzuki, and W. Glöckle. Low-momentum nucleon-nucleon interaction and its application to few-nucleon systems. *Physical Review C*, 70(2):24003, 2004. pages 38

[52] R. Machleidt D. R. Entem. Accurate nucleon-nucleon potential based upon chiral perturbation theory. *Physics Letters B*, 524:1, 2002. pages 39

[53] D. R. Entem and R. Machleidt. Accurate charge-dependent nucleon-nucleon potential at fourth order of chiral perturbation theory. *Phys. Rev. C*, 68(4):041001, Oct 2003. pages 39

[54] B. Jurado, H. Savajols, W. Mittig, A Orr, N, P. Roussel-Chomaz, D. Baiborodin, W.N. Catford, M. Chartier, C.E. Demonchy, Z. Dlouhỳ, et al. Mass measurements of neutron-rich nuclei near the N= 20 and 28 shell closures. *Physics Letters B*, 649(1):43–48, 2007. pages 40

[55] B.A. Brown and W.A. Richter. Magic numbers in the neutron-rich oxygen isotopes. *Physical Review C*, 72(5):57301, 2005. pages 40

[56] G. Hagen, J.S. Vaagen, and M. Hjorth-Jensen. The contour deformation method in momentum space, applied to subatomic physics. *Journal of Physics A Mathematical and General*, 37(38):8991–9021, 2004. pages 47